Ore Geology Reviews 86 (2017) 382–403

Contents lists available at ScienceDirect

Ore Geology Reviews

journal homepage: www.elsevier.com/locate/oregeo

Mineralogical evidence for crystallization conditions and petrogenesis of ilmenite-series I-type granitoids at the Baogutu reduced porphyry Cu deposit (Western Junggar, NW China): Mössbauer spectroscopy, EPM and LA-(MC)-ICPMS analyses

MingJian Cao [a,*], KeZhang Qin [a,*], GuangMing Li [a], Noreen J. Evans [b], Pete Hollings [c], Markus Maisch [d], Andreas Kappler [d]

[a] Key Laboratory of Mineral Resources, Institute of Geology and Geophysics, Chinese Academy of Sciences, P.O. Box 9825, Beijing 100029, China
[b] John de Laeter Center, TIGeR, Applied Geology, Curtin University, Perth, WA 6945, Australia
[c] Geology Department, Lakehead University, 955 Oliver Rd, Thunder Bay, ON P7B 5E1, Canada
[d] Geomicrobiology, Center for Applied Geosciences, University of Tuebingen, Sigwartstrasse 10, 72076 Tuebingen, Germany

ARTICLE INFO

Article history:
Received 9 August 2016
Received in revised form 15 December 2016
Accepted 27 February 2017
Available online 28 February 2017

Keywords:
Mössbauer spectroscopy
LA-(MC)-ICPMS
In situ apatite Nd isotope
Oxygen fugacity
Baogutu reduced porphyry Cu deposit

ABSTRACT

Primary ore-forming minerals retain geochemical signatures of magmatic crystallization information and can reveal the petrochemical conditions prevalent at the time of their formation. The Baogutu deposit is a typical reduced porphyry Cu deposit. Amphibole and biotite $Fe^{3+}/\Sigma Fe$ ratios, minerals (feldspar, biotite, amphibole, zircon and apatite), *in situ* elemental and apatite Nd isotopic compositions were determined by Mössbauer spectroscopy, electron probe microanalysis, and laser ablation multiple-collection inductively coupled plasma mass spectrometry, respectively, to investigate the magma oxidation state, petrogenesis, source features, and to constrain the carbon species at magmatic stages for the intrusive phases. The results show that the primary plagioclase and amphibole in the mineralized diorite to granodiorite porphyry and post ore hornblende diorite porphyry are distinct (An_{26-55} versus An_{60-69}; Mg-hornblende versus tschermakite). In particular, the amphibole shows distinct major and trace element compositions with light rare earth element enrichments and negative Eu anomalies in Mg-hornblende and light rare earth element depletions and no Eu anomalies in tschermakite. All the analyzed biotites are primary igneous phases with a biotite phenocryst profile showing significant variations of Zn, Cr, Sc and Sr from core to rim. These results may indicate the occurrence of mixing between two distinct magmas during mineral formation. Titanium in zircon and Si^* in amphibole thermometries indicate that magma crystallized at >900 °C and continued to ~650 °C. *In situ* apatite Nd isotope ($\varepsilon Nd(t) = 5.6–7.6$, $T_{DM2} = 620–460$ Ma), indicate absence of significant reduced sedimentary contamination and the source of juvenile lower crust. Slightly decreasing $Fe^{3+}/\Sigma Fe$ ratios from biotite and amphibole to whole rock indicate decreasing oxygen fugacity during magma crystallization. Recalculated biotite compositions according to $Fe^{3+}/\Sigma Fe$ ratios indicate fO_2 values of less than Ni-NiO buffer (NNO) which show slightly lower values than that estimated according to zircon/melt distribution coefficients Ce anomalies (~ΔNNO + 0.6). These values are consistent with the features of reduced porphyry Cu deposits. Crystallization of other mineral phases significantly affects the reliability of oxybarometer of zircon/melt distribution coefficients Eu anomalies and Mn contents in apatite. This oxidation state suggests that only CO_2 was present at the magmatic stage, and implies that CH_4 formed during CO_2 reduction occurring later hydrothermal alteration. The alteration of primary amphibole to actinolite released Ti, Al, Fe, Mn, Na and K to the fluid with later precipitation of titanite, albite and minor ilmenite and magnetite during actinolite alteration.

1. Introduction

Typical porphyry Cu deposits are spatially and genetically associated with highly oxidized, magnetite-series I-type granitoids (Hedenquist and Lowenstern, 1994; Qin and Ishihara, 1998;

* Corresponding authors.
E-mail addresses: caomingjian@mail.iggcas.ac.cn (M. Cao), kzq@mail.iggcas.ac.cn (K. Qin).

http://dx.doi.org/10.1016/j.oregeorev.2017.02.033
0169-1368/

Audétat et al., 2004; Sillitoe, 2010; Qin et al., 2014; Cao et al., 2016b) with widespread development of highly oxidized minerals (e.g., anhydrite and hematite), indicative of high fO_2 varying between hematite-magnetite (HM) and Ni-NiO (NNO) buffers (Mungall, 2002; Richards, 2003; Qin et al., 2014; Cao et al., 2016b). The Baogutu deposit in western Junggar, NW China, is a typical reduced porphyry Cu deposit (after Rowins, 2000) given the absence of anhydrite and hematite, predominance of ilmenite over magnetite, widespread occurrence of primary pyrrhotite, and common methane-rich fluid inclusions in ore-forming fluids (Shen et al., 2009; Cao et al., 2014a, 2014b, 2015a). Previous studies have identified three occasionally different intrusive phases within the deposit; diorite with trace fine-grained diorite and gabbro, diorite-granodiorite porphyry, and hornblende diorite porphyry, which all belong to ilmenite-series I-type granitoids (Cao et al., 2016a). Although a lot of studies have been conducted on the Baogutu deposit, mainly focussing on geochemistry and geochronology (Shen et al., 2009, 2010; Wei and Zhu, 2010; Shen and Pan, 2013; Cao et al., 2014a, 2014b, 2015a, 2015b), there are still a number of contentious issues including the oxygen fugacity (Wei et al., 2009; Wei and Zhu, 2010; Shen and Pan, 2013; Cao et al., 2014a, 2015b, 2016a), the detailed crystallization processes and the petrogenesis of the granitoids (Wei and Zhu, 2010; Shen and Pan, 2013; Cao et al., 2016a), and also the carbon species of C (CO_2 or CH_4) during magma crystallization (Shen et al., 2010; Shen and Pan, 2013; Cao et al., 2014b, 2016a).

Felsic rocks are composed of major rock-forming minerals (e.g., plagioclase, amphibole, biotite, feldspar, quartz) and trace accessory minerals (e.g., zircon, apatite, titanite) which can record the physiochemical conditions of the magma (Boomeri et al., 2010; Ridolfi et al., 2010; Bath et al., 2013), crystallization processes (Davidson and Tepley, 1997; Tepley et al., 2000; Ruprecht and Wörner, 2007; Qin et al., 2009; Shcherbakov et al., 2011; Cao et al., 2012, 2014c), and also the source information. The proportion of Fe^{3+} and Fe^{2+} in primary Fe-rich minerals (e.g., amphibole, biotite) is a very important indicator of magma oxygen fugacity, and can be precisely determined by Mössbauer spectroscopy (Rancourt et al., 1992; Gunter et al., 2003). Due to the extremely slow diffusivity of rare earth elements (REEs) in zircon (Cherniak et al., 1997a,b) and also in apatite (Watson et al., 1985; Cherniak, 2000), zircon and apatite retain primary compositions and can be used to constrain the oxidation state of the magma (Ballard et al., 2002; Trail et al., 2012). In addition, laser ablation multiple-collection inductively coupled plasma mass spectrometry (LA-MC-ICPMS) has been successfully used to determine *in situ* Nd isotopes in apatite (Foster and Vance, 2006; Yang et al., 2008, 2014), which could be used to constrain the magma petrogenesis.

In order to resolve the aforementioned issues and to determine if other minerals record magmatic crystallization and petrochemical signatures, we quantified $Fe^{3+}/\Sigma Fe$ ratios of amphibole and biotite, *in situ* major and trace elemental compositions of feldspar, biotite, amphibole, zircon and apatite, and also *in situ* apatite Nd isotopic compositions at the Baogutu deposit, using Mössbauer spectroscopy, electron probe microanalysis (EPMA) and LA-(MC)-ICPMS.

2. Geological setting

The Baogutu reduced porphyry copper deposit is situated in the southeast of western Junggar, in the western region of the Central Asian Orogenic Belt (Fig. 1a). In this area, there are different types of Carboniferous to Early Permian mafic to felsic intrusions including large batholiths, small stocks, high-Mg dioritic dikes, charnockites, tholeiitic basalts, which are probably related to spreading ridge subduction (e.g., Zhang et al., 2004; Tang et al., 2010). The Baogutu deposit is hosted in a small dioritic stock (~0.6 km^2) which was emplaced into the Lower Carboniferous Xibeikulas and Baogutu formations (Fig. 1b), and contains 63×10^4 t of Cu averaging 0.28 wt.%, and 14 t of Au averaging 0.1 ppm (Zhang et al., 2006). Detailed characteristics of the deposit and ore body are given in Cao et al. (2014a). From oldest to youngest, three main intrusive phases are recognized (Cao et al., 2016a): (1) diorite major component (~320 Ma), (2) diorite porphyry and granodiorite porphyry (312–310 Ma), and (3) hornblende diorite porphyry (306 Ma). Dating molybdenite (Re-Os) and hydrothermal biotite ($^{39}Ar/^{40}Ar$) showed that the mineralization occurred at ~310 Ma (Song et al., 2007; Shen et al., 2012; Li et al., 2014), contemporaneous with the emplacement of the diorite and granodiorite porphyry (312–310 Ma; Li et al., 2014; Cao et al., 2016a). Although extremely reduced CH_4-rich fluid inclusions have been commonly reported in the Baogutu deposit (Shen et al., 2010; Cao et al., 2014a, 2014b, 2015a), many studies have argued that the granitoids show highly oxidized characteristics of magnetite-series I-type granitoids (Wei et al., 2009; Wei and Zhu, 2010; Shen and Pan, 2013). However, our recent detailed studies indicated that all the granitoids belong to relatively reduced ilmenite-series I-type granitoids, characterized by widespread primary pyrrhotite without anhydrite or hematite, dominant ilmenite over magnetite, low whole rock magnetic susceptibility and low whole rock Fe_2O_3/FeO ratios characteristics (Cao et al., 2016a). In addition, limited zircon REE compositions also indicated a relatively lower oxidation state for the granitoids from the Baogutu deposit relative to other large to giant porphyry Cu deposits of the Central Asian Orogenic Belt (Shen et al., 2015). All rocks have restricted whole rock Sr-Nd and zircon Hf-O isotopic compositions ($(^{87}Sr/^{86}Sr)_i$ = 0.7036 to 0.7040, ε_{Nd} (t) = +6.3 to +7.8, ε_{Hf} (t) = +10.7 to +15.8, $\delta^{18}O$ = 5.3 to 7.4‰; Cao et al., 2016a), indicating a primitive source without significant ancient continental crust or sediment contamination. Detailed plagioclase elemental and Sr isotopic analyses show zoning consistent with repeated, more mafic magma recharge into the felsic magma chamber (Cao et al., 2014c). Systematic fluid inclusions Laser-Raman analyses and CO_2-CH_4 C isotopes suggest that magmatic CO_2 was probably reduced to CH_4 by Fischer–Tropsch type reactions occurring during hydrothermal alteration (Cao et al., 2014b).

Major elements compositions of feldspar, biotite and amphibole were determined on thin sections of diorite (ZK211-295, ZK202-205 and ZK209-284), granodiorite porphyry (ZK204-17, ZK202-40, ZK205-293 and BCK2-1) and hornblende diorite porphyry (ZK211-141 and ZK213-218). Only primary feldspar, biotite and amphibole from ZK209-284, BCK2-1 and ZK213-218 were further analyzed for *in situ* trace elements in thin sections (see Fig. 2). Magmatic biotite and amphibole selected from both diorite (ZK603-109 and ZK603-271) and granodiorite porphyry (BCK2-1 and ZK202-40) were analyzed by Mössbauer spectroscopy to quantify the $Fe^{3+}/\Sigma Fe$ ratios. Due to a scarcity of grains, *in situ* zircon and apatite trace elements were analyzed on individual crystals separated from the diorite (ZK003-233, BHS and BTC196), fine-grained diorite (BXS), diorite porphyry (BSB), granodiorite porphyry (BCK2-1) and hornblende diorite porphyry (ZK213-218). In addition, apatite grains from ZK003-233 and BCK2-1 were determined for *in situ* Nd isotope composition. All the samples information and the corresponding analyzed minerals and analytical methods in this study are summarized in Table 1.

3. Analytical methods

Mössbauer spectroscopy on biotite and amphibole was done at the University of Tuebingen following protocols from previous studies (Larese-Casanova et al., 2010; Muehe et al., 2013). Samples were loaded into Plexiglas holders (area 1 cm^2) forming a thin disc.

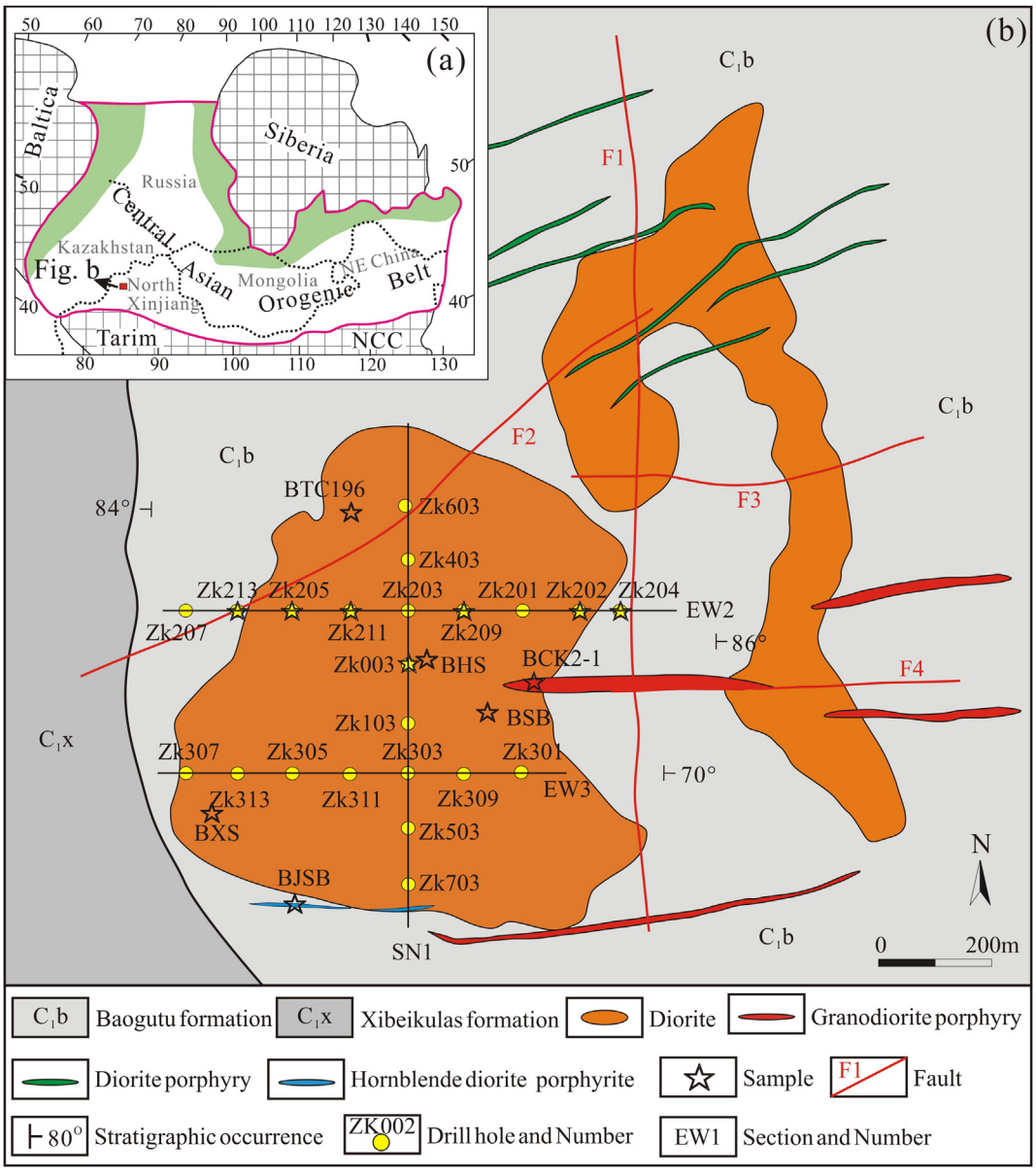

Fig. 1. (a) Location of the study area in the Central Asian Orogenic Belt modified after Jahn (2004). (b) Geological map of the Baogutu porphyry copper deposit showing the different intrusions and sample locations, modified after Zhang et al. (2006).

Sample holders were then loaded into a closed-cycle exchange gas cryostat (Janis cryogenics) to minimize exposure to air during measurement. Spectra were collected at 77 K using a constant acceleration drive system (WissEL) in transmission mode with a ^{57}Co/Rh source. All spectra were calibrated against a 7 μm thick α-^{57}Fe foil that was measured at room temperature. Analysis was carried out using Recoil (University of Ottawa) and the Voigt Based Fitting (VBF) routine (Rancourt and Ping, 1991). The half width at half maximum (HWHM) was constrained to 0.123 mm/s during fitting.

The major element compositions of minerals were measured at the Institute of Geology and Geophysics, Chinese Academy of Sciences (IGGCAS) in Beijing, using a JEOL-JXA8100 electron microprobe operated in wavelength dispersive spectrometer mode. The operating conditions were 15 kV accelerating voltage, 10 nA beam current and 3 μm probe beam with counting times of 20 s for Si, Ti, Al, Fe, Mn, Mg, Na, K, S and Cl, 40 s for F, and 10 s for Ca and P at their characteristic X-ray line. The following natural minerals and synthetic oxides were used for calibration: apatite (P), barite (S), diopside (Ca and Si), rutile (Ti), jadeite (Al), garnet (Fe), bustamite (Mn), jadeite (Na), K-feldspar (K), pyrope (Mg), chromite (Cr), tugtupite (Cl) and fluorite (F). All data were corrected using the atomic number-absorption-fluorescence procedure.

In situ trace elemental analyses of biotite, amphibole, feldspar in thin section and apatite and zircon grain separates in epoxy mounts utilized an Agilent 7500a quadruple inductively coupled plasma mass spectrometer (ICPMS) coupled to a 193 nm excimer ArF laser ablation system at the IGGCAS. The detailed analytical technique is similar to that described in Xie et al. (2008). Helium gas was flushed to minimize aerosol deposition around the ablation site, and mixed with argon gas downstream of the ablation cell. Analysis was performed with a spot size of 44 μm, repetition rate of 6 Hz, and energy density of ~10 J/cm^2. All measurements were performed in time-resolved analysis mode utilizing peak jumping with 1 point per mass peak. Each spot analysis consisted of approximately 30 s of background acquisition and 60 s of sample data acquisition. BCR-2G, BHVO-2G and BIR-1G were used as exter-

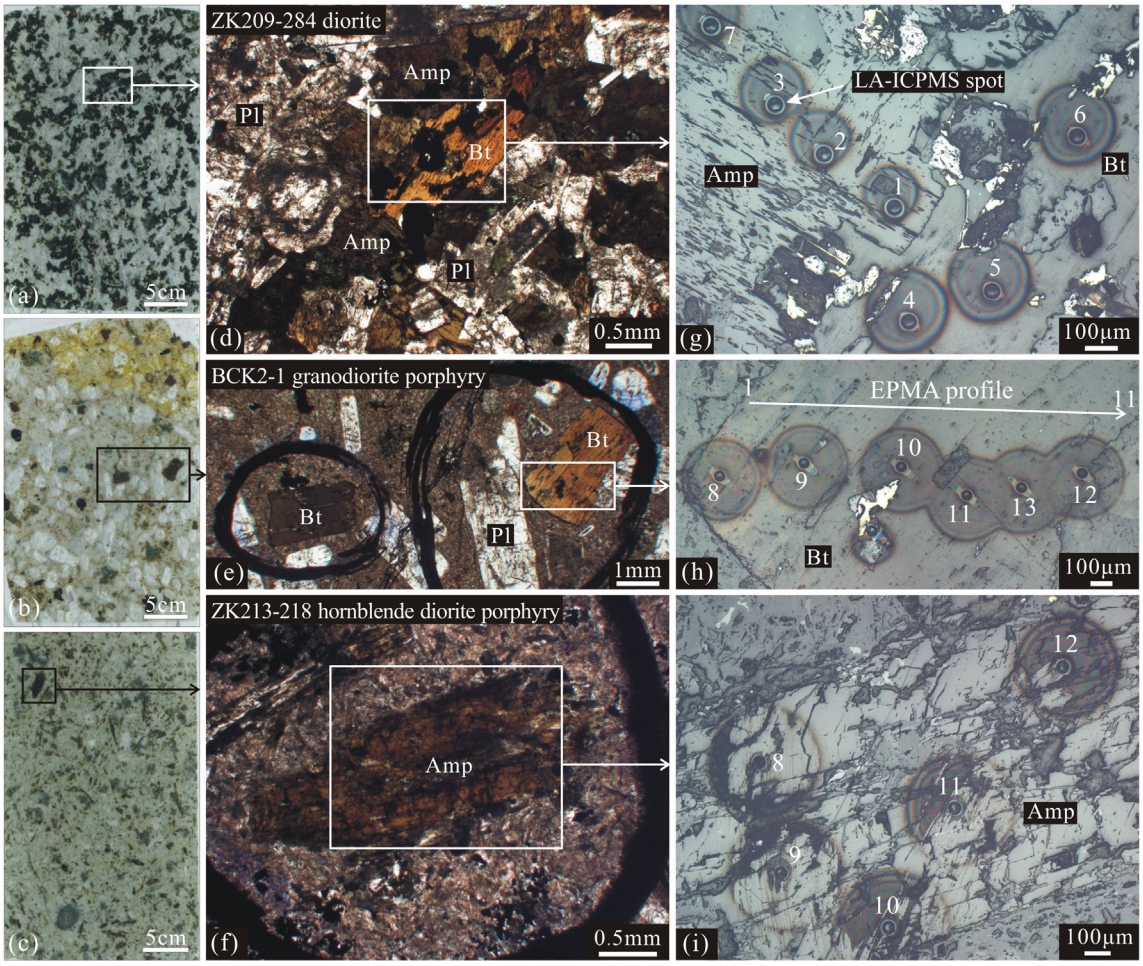

Fig. 2. (a–c) Photographs of ZK209-284 diorite, BCK2-1 granodiorite porphyry and ZK213-218 hornblende diorite porphyry, (d–f) Enlarged microphotographs of (a–c) (plane-polarized light), (g–i) Enlarged microphotographs of (d–f) showing the position of EPMA and LA-ICPMS spots (reflected light). Abbreviations: Amp, amphibole; Bt, biotite; Pl, plagioclase.

Table 1
Summary of all the samples information and the corresponding analyzed minerals and analytical methods in this study.

Lithology	Age (Ma)†	Sample	Depth‡ (m)	Analyzed minerals	Analytical Methods
D	~320	ZK211-295	586	Amp, Bt, Kfs	EPMA
	~320	ZK202-205	477	Amp, Bt,	EPMA
	~320	ZK209-284	569	Amp, Bt	EPMA, LA-ICPMS
	~320	ZK603-109	221	Amp, Bt	MS
	~320	ZK603-271	549	Amp, Bt	MS
	320.5	ZK003-233	473	Ap, Zrc	LA-(MC)-ICPMS
	320.3	BHS	0	Zrc	LA-ICPMS
	321.1	BTC196	0	Zrc	LA-ICPMS
FGD	320.6	BXS	0	Zrc	LA-ICPMS
DP	312.6	BSB	0	Zrc	LA-ICPMS
GDP	~310	ZK204-17	43	Amp, Bt	EPMA
	~310	ZK202-40	141	Bt, Kfs	MS, EPMA
	~310	ZK205-293	597	Bt	EPMA
	310.1	BCK2-1	0	Amp, Ap, Bt, Zrc	MS, EPMA, LA-(MC)-ICPMS
HDP	~305.6	ZK211-141	281	Amp, Kfs, Pl	EPMA
	~305.6	ZK213-218	527	Amp, Ap, Pl, Zrc	EPMA, LA-ICPMS

† All the ages are cited from Cao et al., (2016a).
‡ Depth is the location below the surface. Abbreviations: D: diorite; DP, diorite porphyry; FGD, fine-grained diorite; GDP, granodiorite porphyry; HDP, hornblende diorite porphyry; Amp, amphibole; Ap, apatite; Bt, biotite; Kfs, K-feldspar; Pl, plagioclase; Zrc, zircon; EPMA, electron probe microanalysis; MS, Mössbauer spectroscopy; LA-(MC)-ICPMS, laser ablation (multiple-collection) inductively coupled plasma mass spectrometry.

nal standards. SiO_2 contents determined by EPMA were used as an internal standard for biotite, amphibole, feldspar, and SiO_2 value of 32.78 as internal standards for zircon. Raw counts were processed offline and data-reduction and concentration calculations were then performed using Glitter (Griffin et al., 2008). Accuracy of trace element concentrations is better than 5% for most elements based

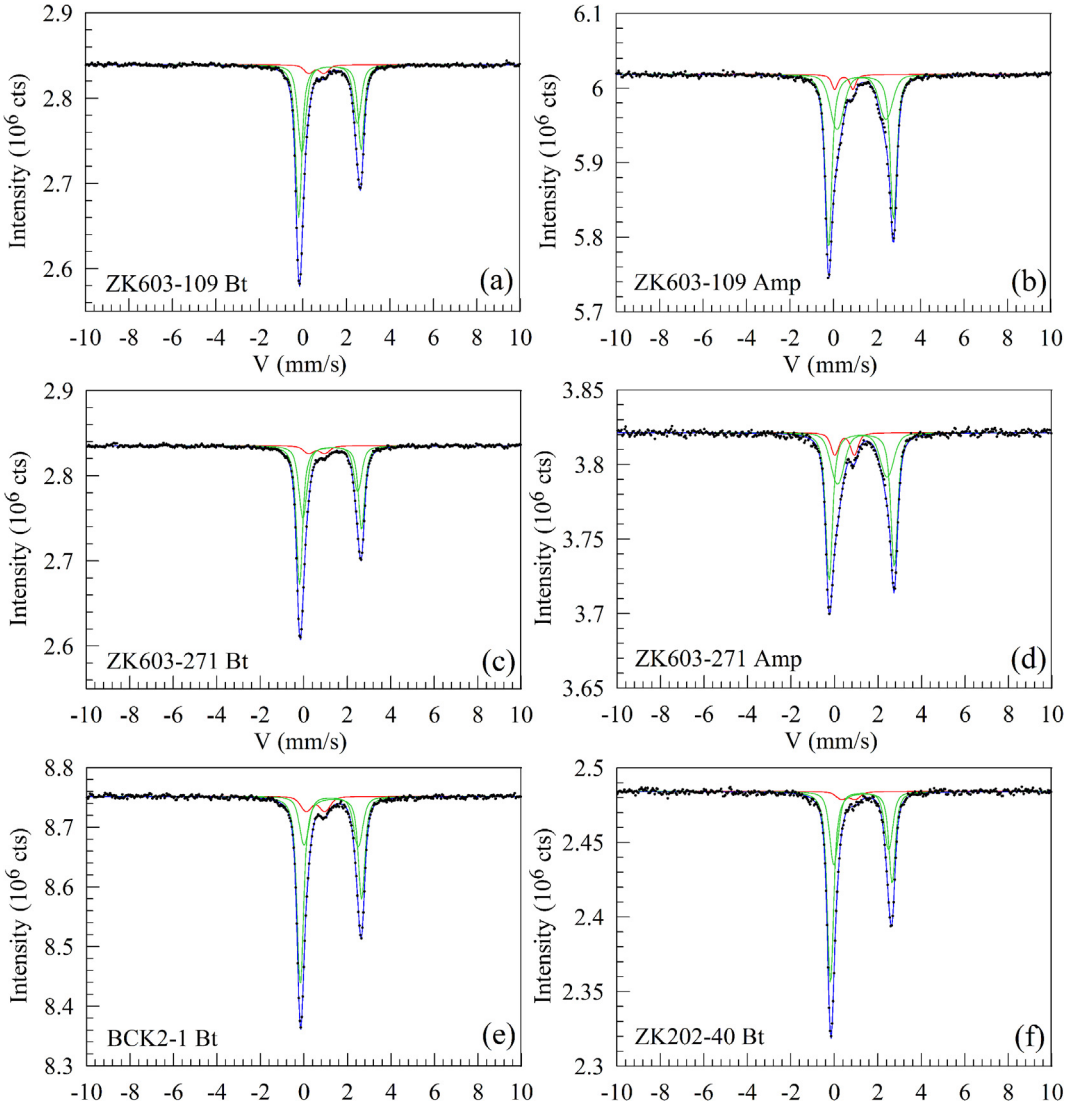

Fig. 3. Mössbauer spectra collected at 77 K for diorite ZK603-109 biotite (a) and amphibole (b), diorite ZK603-271 biotite (c) and amphibole (d), granodiorite porphyry BCK2-1 biotite (e) and ZK202-40 biotite (f). All spectra are characterized by a predominant doublet (Db1, Db2) for Fe^{2+} and a weakly pronounced doublet (Db3) for Fe^{3+}. Black dots represent measured spectra data, blue line represents 3-fit model, green lines represent best fit for doublets Db1 and Db2, and pink lines represent best fits for doublet Db3. (For interpretation of the references to color in this figure legend, the reader is referred to the web version of this article.)

on repeated analyses of the reference materials. LA-ICPMS analytical results for reference materials are listed in Supplementary Table A.1.

In situ Nd isotope compositions of apatite grains were measured over previous trace element analysis positions for ZK003-233 (diorite) and BCK2-1 (granodiorite porphyry) using laser ablation coupled to a Neptune multi-collector ICPMS at the IGGCAS. A spot size of 160 μm was employed with a 8 Hz repetition rate and an energy density of 15 J/cm^2. Prior to analyses, the Neptune MC-ICPMS was tuned and optimized for maximum sensitivity using the JNdi-1 standard solution. International apatite standard Durango Chew (Durango), Madagascar (MAD) and Otter Lake were used to evaluate the reliability of the analysis system and calibration technique. Each spot analysis consisted of approximately 60 s data acquisition. The detailed *in situ* Nd isotopic analytical technique has been described in Yang et al. (2008, 2014). Apatite standards Nd isotopic compositions show values of $^{143}Nd/^{144}Nd = 0.51248 \pm 1$ (1σ, n = 20) for Durango, $^{143}Nd/^{144}Nd = 0.51133 \pm 1$ (1σ, n = 10) for MAD, $^{143}Nd/^{144}Nd = 0.51194 \pm 1$ (1σ, n = 10) for Otter Lake which are well within the accepted Nd isotopic composition for Durango $^{143}Nd/^{144}Nd = 0.512493 \pm 21$ (2σ), for MAD $^{143}Nd/^{144}Nd = 0.511348 \pm 16$ (2σ), and for Otter Lake $^{143}Nd/^{144}Nd = 0.511940 \pm 9$ (2σ) analyzed by both TIMS and solution MC-ICPMS analyses (Yang et al., 2014). Apatite standards LA-MC-ICPMS Nd isotopic analytical results are listed in Supplementary Table A.2.

4. Results

4.1. Mössbauer spectroscopy

Samples were measured at 77 K and are all characterized by a predominant doublet (Db) and a poorly pronounced second doublet that overlaps and intensifies the first peak of the first doublet forming a second small peak in the overlay (Fig. 3). All spectra were fitted by a 3-fit model using three doublet-fits in total, two doublets for Fe^{2+} species (Db1, Db2), and one doublet for Fe^{3+} (Db3). The asymmetry in peak positions and area, that can be observed in biotite (Chandra et al., 1978; Aldridge et al., 1991), was accounted for by allowing Db1 and Db2 to fit asymmetrically. The results of Mössbauer analysis and estimated proportion of Fe^{2+} and Fe^{3+} are summarized in Table 2.

Table 2
The results of Mössbauer analyses and estimated proportions of Fe^{2+} and Fe^{3+} in biotite and hornblende from the Baogutu deposit.

Sample	Lithology	Mineral	Phase	CS (mm/s)	ΔE_Q (mm/s)	Fe^{2+} (%)	Fe^{3+} (%)	χ^2
ZK603-109	diorite	Bt	Db1	1.25	2.87	52.9		0.78
			Db2	1.23	2.56	41.9		
			Db3	0.62	0.69		5.2	
		Hbl	Db1	1.27	2.98	61.3		1.10
			Db2	1.28	2.25	33.6		
			Db3	0.47	0.84		5.1	
ZK603-271	diorite	Bt	Db1	1.24	2.85	57.2		0.64
			Db2	1.22	2.52	37.2		
			Db3	0.59	0.74		5.6	
		Hbl	Db1	1.25	2.99	57.0		0.71
			Db2	1.27	2.28	33.2		
			Db3	0.46	0.90		9.8	
BCK2-1	granodiorite porphyry	Bt	Db1	1.24	2.81	62.8		0.63
			Db2	1.25	2.48	27.9		
			Db3	0.53	0.86		9.3	
ZK202-40	granodiorite porphyry	Bt	Db1	1.24	2.80	72.1		0.66
			Db2	1.30	2.38	24.0		
			Db3	0.46	0.87		3.9	

Bt, biotite; Hbl, hornblende; CS, Center shift; ΔEQ, Quadrupole splitting; χ2, goodness of fitting.

The hyperfine field parameters for the dominant doublets Db1 and Db2 in all samples showed generally high values for the center shift (CS) ranging from 1.22 to 1.30 mm/s and the quadrupole splitting (ΔE_Q) ranging from 2.25 to 2.99 mm/s. These parameters can be attributed to the presence of Fe^{3+} in the mineral phase. The hyperfine field parameters for the poorly pronounced doublet Db3 show generally lower values for CS ranging from 0.46 to 0.62 mm/s and ΔE_Q ranging from 0.69 to 0.90 mm/s. The predominance of Db1 and Db2 over Db3 indicates that Fe^{2+} is the major form in all samples with a relatively low concentration of Fe^{3+}. Four biotite samples show similar spectra, while the two hornblende samples (ZK603-271 and ZK603-109) show slightly different spectra (Fig. 3), with a generally less pronounced asymmetric shape for the doublets. In particular, the Fe^{2+} doublet showed a wider range and a characteristic shoulder feature at around $\Delta E_Q = 0.0$ and 2.2 mm/s that mainly corresponds to the hyperfine field parameters of hornblende (Mitra and Bansal, 1975).

With respect to the site population properties of Db1 and Db2 in contrast to Db3 (Table 2), the Fe^{2+} clearly dominates over the Fe^{3+} in all samples. The absolute site population and calculated relative abundance of Fe^{2+} was remarkably larger in all samples with values >89%, while the calculated proportions of Fe^{3+} show values of <10% for all samples.

4.2. EPMA results

All analyzed chemical compositions of amphibole, feldspar, biotite and apatite are presented in Supplementary Table A.3.

All amphiboles show minor contents of K_2O (<0.02 to 0.58 wt.%) and MnO (below detection limit to 0.48 wt.%) (Table A.3). The analyzed amphiboles from diorite, granodiorite porphyry and hornblende diorite porphyry show distinct variations and can be classified as type I (Mg-hornblende), type II (tschermakite) and type III (actinolite) according to Leake et al. (1997) (Fig. 4). Type I and II are primary amphibole, whereas type III is the product of alteration.

The plagioclase in hornblende diorite porphyry show significant higher An values ($An_{60-69}Ab_{39-30}$; Fig. 5a), relative to the plagioclase in diorite and granodiorite porphyry ($An_{26-55}Ab_{70-44}$; Cao et al., 2014c). The K-feldspar in hornblende diorite porphyry show similar Or variations (Or_{82-97}; Fig. 5a) with that in diorite and granodiorite porphyry (Or_{82-97}; Cao et al., 2014a).

Biotites from the diorite and granodiorite porphyry show similar compositions with TiO_2 contents of 2.89 to 5.35 wt.%, FeO of 15.19 to 19.92 wt.%, MnO of 0.01 to 0.22 wt.%, MgO of 10.54 to 13.70 wt.%, and K_2O of 7.69 to 9.43 wt.% (Table A.3). On the $10 * TiO_2 - (FeO + MnO)$-MgO discrimination diagram (after Nachit et al., 2005), all the biotite fall within the field of primary biotite (Fig. 5b).

All the analyzed apatites show relatively high contents of F (mean = 3.06 ± 0.29, 1σ, n = 40, mean = 2.29 ± 0.20, 1σ, n = 40; mean = 2.62 ± 0.64, 1σ, n = 30), low contents of Cl (mean = 0.35 ± 0.12, 0.85 ± 0.20, and 0.30 ± 0.23) and SiO_2 (0.15 ± 0.07, 0.15 ± 0.13 and 0.19 ± 0.22) for ZK003-233 diorite, BCK2-1 granodiorite porphyry and ZK213-218 hornblende diorite porphyry, respectively (Table A.3). Thus, all apatite grains are belonging to fluorapatite (Fig. 5c).

4.3. LA-ICPMS results

Forty-two *in situ* trace element analyses of silicate minerals including amphibole, biotite and feldspar are listed in Table 3. A total of one hundred and fifteen zircon grains were analyzed from the diorite (ZK003-233, BHS, BTC196), fine-grained diorite (BXS), diorite porphyry (BSB), granodiorite porphyry (BCK2-1) and hornblende diorite porphyry (BJSB), as summarized in Table 4. The results of fifty-five apatite grains from diorite ZK003-233, granodiorite porphyry BCK2-1 and hornblende diorite porphyry ZK213-218 are given in Table 5.

Compared with the amphibole in the hornblende diorite porphyry (n = 8), the amphibole in the diorite (n = 10) show higher contents of Zn (118 to 152 ppm), Zr (39.8 to 112 ppm), Nb (2.87 to 6.54 ppm) and REEs (116 to 219 ppm), but lower contents of V (256 to 393 ppm), Cr (48.8 to 96.9 ppm), Ni (113 to 143 ppm) and Sr (44.7 to 147 ppm) (Table 3). Plagioclase in the hornblende diorite porphyry shows low contents of Sc (1.19 ppm), Rb (1.5 ppm), Ga (23.3 ppm) and REEs (~4.94 ppm), but high contents of Ba (167 ppm) and Sr (2119 ppm) (Fig. 5a, b). K-feldspar in the hornblende diorite porphyry has low Ga (5.08 to 11.2 ppm), Sr (473 to 641 ppm), and REEs (Fig. 5a, b), but higher contents of Rb (151 to 673 ppm) and Ba (1430 to 3356 ppm) (Table 3). Biotite in both the diorite (n = 10) and granodiorite porphyry (n = 10) show variable contents of trace elements, such as Cr (93.7 to 854 ppm), Zn (71.7 to 147 ppm), Sc (5.16 to 24.1 ppm), Ba (1995 to 8145 ppm) (Table 3). All 115 zircon analyses yielded similar trace element compositions with wide variations of Ti (2.19 to 38.3 ppm), Y (492 to 3038 ppm), Pb (3.32 to 27.1 ppm), Th (33.0 to 408 ppm), U (48.0 to 365 ppm) with Th/U ratios of 0.35 to 1.56 (Table 4). Apatite grains from the diorite, granodiorite porphyry and hornblende

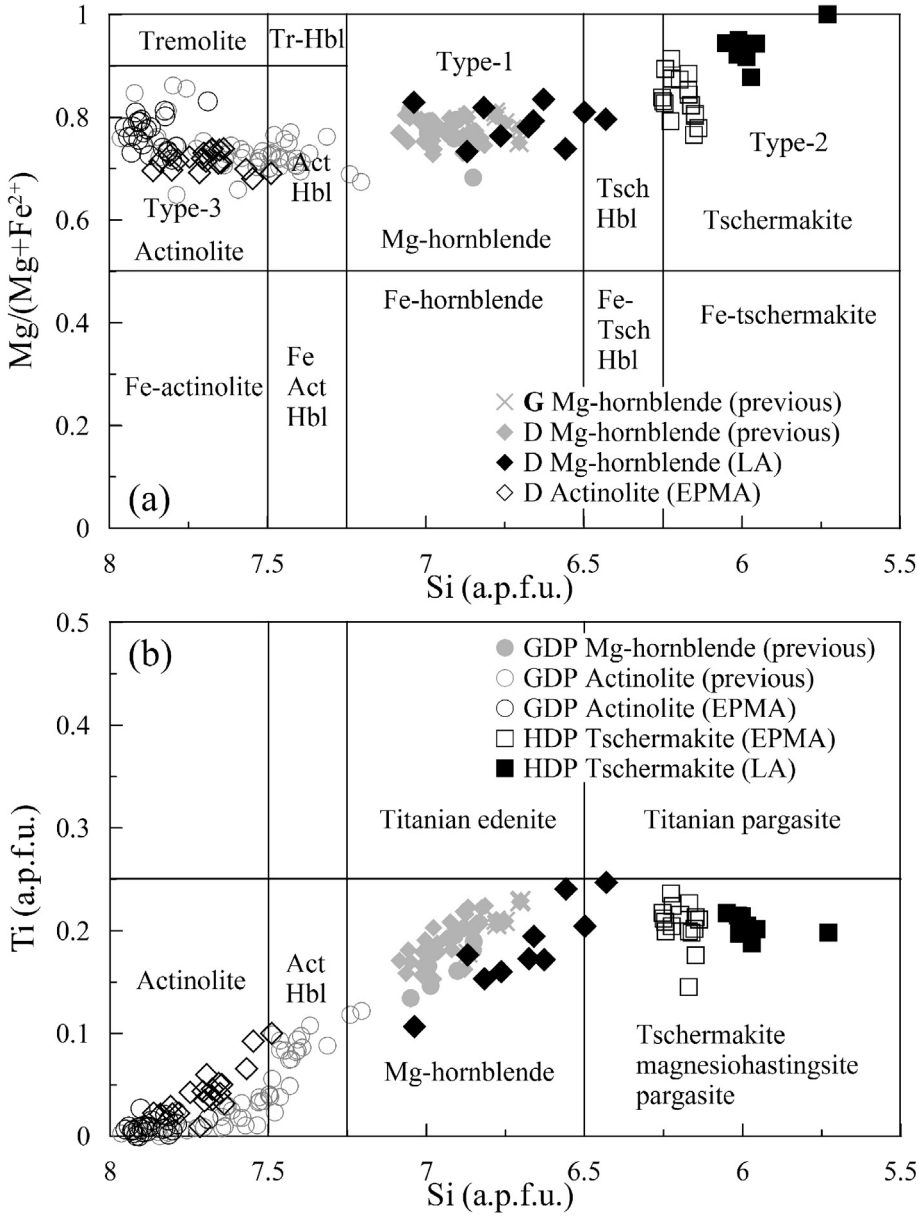

Fig. 4. Classification diagrams for calcic-amphiboles from Baogutu deposit after Leake et al. (1997). Si (a.p.f.u.) versus Mg/(Mg + Fe^{2+}) (a) and Ti (a.p.f.u.) (b) for Ca > 1.0 and $(Na + K)_A$ < 0.5. Act, Actinolite; Hbl, Hornblende; Tsch, Tschermakite, GDP, granodiorite porphyry; D, diorite; G, gabbro; HDP, hornblende diorite porphyry. The previously published data of calcic-amphiboles are from Dai et al. (2010), Wei and Zhu (2010) and Shen and Pan (2013). a.p.f.u. = atoms per formula unit.

diorite porphyry show variable contents of trace elements, such as Sr (140 to 603 ppm), Y (119 to 1566 ppm), V (59.4 to 2.65 ppm), Ga (32.7 to 1.50 ppm), Pb (6.91 to 0.32 ppm), Th (72.8 to 1.36 ppm) and U (12.4 to 0.10 ppm) (Table 5).

The chondrite-normalized REE patterns for feldspar, amphibole, zircon and apatite show distinct features (Fig. 6). The feldspar including both plagioclase and K-feldspar shows significant positive Eu anomalies and right-inclined light REE (LREE) distribution patterns (Fig. 6a, b). The type I and type II amphiboles show obviously different characteristics, with LREE enriched and negative Eu anomalies in type I amphibole but LREE depleted and lack of Eu anomalies in type II amphibole (Fig. 6c). All the zircons show left-inclined REE distribution patterns with significant positive Ce but negative Eu anomalies (Fig. 6d, e, f). Apatite grains show obvious right-inclined REE distribution patterns with negative Eu anomalies (Fig. 6g, h). In addition, type I amphiboles show similar REE distribution patterns but lower contents of heavy REE (HREE) with previously published primary titanite (Fig. 6i, Cao et al., 2015a).

4.4. Nd isotopic composition of apatite

Forty *in situ* Nd isotopic compositions of apatite (diorite ZK003-233 and granodiorite porphyry BCK2-1) are given in Table 6. The analyzed apatite from diorite and granodiorite porphyry show similar $^{147}Sm/^{144}Nd$ values of 0.0974 to 0.1253 and 0.0973 to 0.1142, $(^{143}Nd/^{144}Nd)_i$ values of 0.51253 to 0.51262 and 0.51252 to 0.51259 (Fig. 7a), corresponding to εNd(t) values of 5.9 to 7.6 (mean = 6.7 ± 0.5, 1σ, n = 24), 5.6 to 6.9 (mean = 6.4 ± 0.4, 1σ, n = 16), T_{DM2} ages of 460 to 600 Ma and 510 to 620 Ma (Fig. 7b), respectively.

4.5. Temperature of crystallization

Two independent geothermometers were applied in order to estimate the crystallization temperature of different mineral phases: Ti in zircon thermometry (after Watson et al., 2006; Ferry and Watson, 2007) and Si* in amphibole thermometry (see

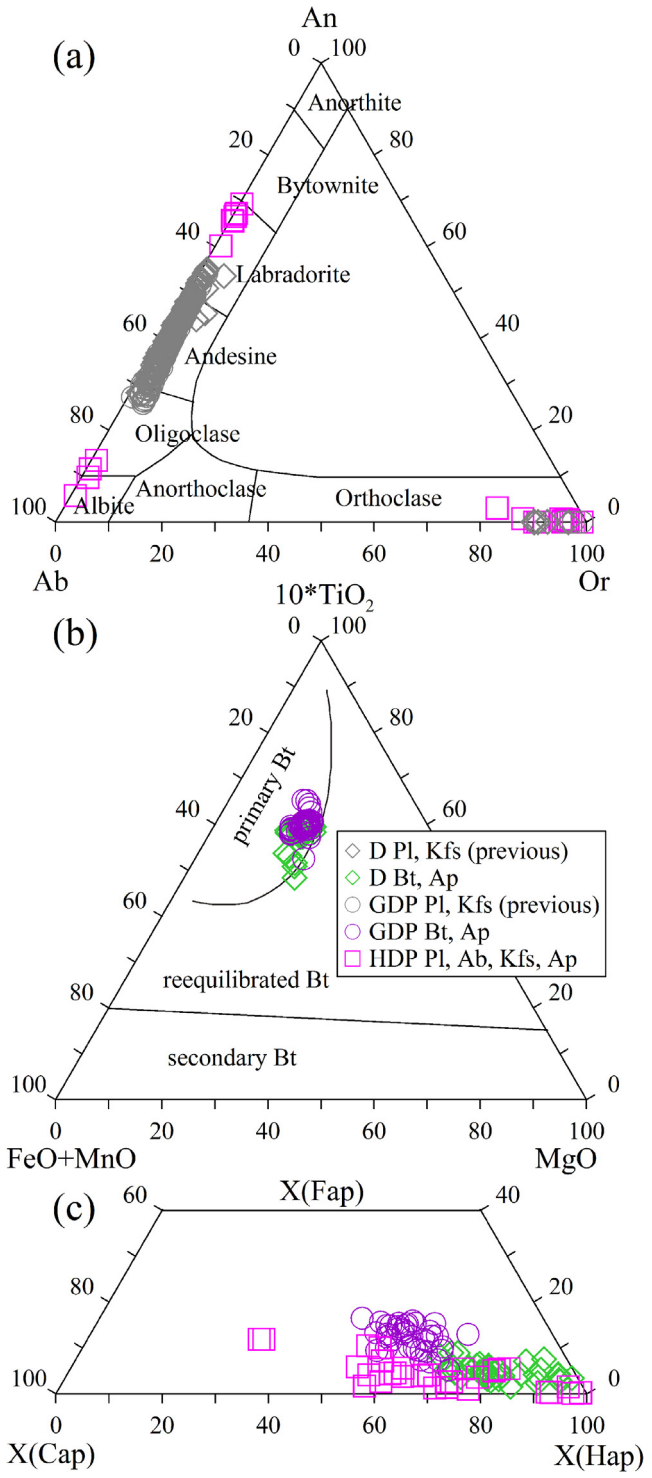

Fig. 5. (a) Ab-Or-An classification diagram for feldspar, (b) $10*TiO_2$ – (FeO + MnO)-MgO discrimination diagram for biotite (Bt) after Nachit et al. (2005), and (c) X(Fap)-X(Cap)-X(Hap) discrimination diagram for apatite (Ap) for the Baogutu granitoids. The previous data of plagioclase (Pl) and K-feldspar (Kfs) are from Cao et al. (2014a, 2014c).

the definition of Si^* in Ridolfi et al., 2010) (Fig. 8). Cao et al. (2014a) showed the occurrence of rutile and quartz in all phases, indicating Ti and Si activities of 1. The Ti in zircon thermometry show wide variations with values ranging of 668 to 826 °C (768 ± 37 °C; n = 54, 1σ) for the diorite, 761 to 882 °C (810 ± 31 °C; n = 23) for the fine-grained diorite, 630 to 792 °C (717 ± 45 °C; n = 13) for the diorite porphyry, 683 to 752 °C (728 ± 21 °C; n = 15) for the granodiorite porphyry, and 622 to 800 °C (743 ± 57 °C; n = 10) for the hornblende diorite porphyry (Fig. 8a). The results of Si^* in amphibole thermometry show temperature variations of 786 to 923 °C (855 ± 41 °C; n = 10, 1σ) for the diorite and 957 to 1005 °C (972 ± 22 °C; n = 22) for the hornblende diorite porphyry (Fig. 8b). Thus, amphibole crystallized earlier than zircon, which is consistent with microscope-based observations that the zircon occurs interstitially with plagioclase and quartz or in the matrix in the porphyry, and amphibole occurs as large euhedral crystals or as large phenocrysts. The magma started to crystallize at >900 °C and continued to crystallize until ~650 °C with the major crystallization period between 850 and 700 °C, consistent with temperatures calculated by zircon saturation thermometry and apatite saturation thermometry (Cao et al., 2016a).

5. Discussion

5.1. Element diffusion in different magmatic mineral phases

If elements or isotopes in minerals diffuse quickly after crystallization, their compositions could be significantly altered by diffusional loss or exchange with other phases, and thus may not retain the signatures inherited at the time of crystallization. In order to check the elemental diffusion capability in apatite, plagioclase, zircon and titanite, we adopted a simple model, as illustrated by Cherniak (2005), in which all the mineral grains are treated as spheres with radii a and an initial uniform concentration C1, and are exposed to a medium with concentration C0. According to Crank (1975), when the dimensionless parameter Dt/a^2 (where D is the diffusion coefficient and t is the time) is higher 0.03, the concentration at the center of the sphere is affected by the surrounding medium. We plot curves of $Dt/a^2 = 0.03$ for different elements with an effective diffusion radius of 75 μm for apatite, titanite and zircon, and 400 μm for plagioclase in Fig. 9. Above these curves, the initial elemental composition will not be changed. Samarium in apatite and strontium in plagioclase will diffuse much faster than REEs in apatite, titanite and zircon and also Mn in apatite (Fig. 9). Combined with all published whole rock TIMS Sr-Nd isotope (Shen et al., 2009; Tang et al., 2010; Shen and Pan, 2013; Cao et al., 2016a), *in situ* titanite Nd (Cao et al., 2015b) and plagioclase Sr isotope data (Cao et al., 2014c), similar compositions were observed for whole rock TIMS and *in situ* mineral (plagioclase and titanite) LA-MC-ICPMS results (Figs. 7b, 9), suggesting the immobility of Sm in apatite and Sr in plagioclase. Thus, REEs in accessory minerals (e.g., apatite, zircon and titanite), Mn in apatite, and Sr in titanite and plagioclase will be immobile, and the compositions of the above elements in corresponding mineral phases should retain primary features and can be used to reveal information about conditions at the time of crystallization.

5.2. Oxidation state of granitoids

5.2.1. Oxidation state of granitoids revealed by zircon

Due to the extremely slow diffusivities for most elements in zircon (Fig. 9; Cherniak et al., 1997a,b), zircon should retain primary crystallization features. Among the REEs, Ce occurs as Ce^{4+} and Ce^{3+}, and Eu as Eu^{3+} and Eu^{2+} under magmatic conditions. Due to their similar ionic radii and charge in eightfold coordination (Ce^{4+} 0.97 Å, Eu^{3+} 1.066 Å) to Zr^{4+} (0.84 Å), Ce^{4+} and Eu^{3+} are incorporated preferentially into zircon relative to Ce^{3+} (r = 1.143 Å) and Eu^{2+} (r = 1.25 Å) (Shannon, 1976). However, the partition coefficients of REEs depend on the oxidation state of the magma, crystallization temperature and melt compositions (Hanchar et al., 2001; Luo and Ayers, 2009). In pioneering work, Onuma et al. (1968)

Table 3
In situ amphibole, biotite and feldspar trace element compositions (in ppm) determined by LA-ICPMS on thin sections from the Baogutu deposit.

Spot	Min.	Sc	V	Cr	Ni	Zn	Ga	Ge	Rb	Sr	Y	Zr	Nb	Sn	Ba
ZK209-284 diorite															
LA-1	Hbl	43.4	326	81.7	120	128	14.9	1.80	1.09	94.9	27.8	72.3	3.49	1.91	79.1
LA-2	Hbl	47.4	317	56.1	128	140	15.1	1.92	0.92	101	25.8	79.9	3.40	2.31	96.0
LA-3	Hbl	82.4	393	96.7	143	132	17.0	2.59	1.12	147	49.7	112	6.21	3.42	153
LA-7	Hbl	43.2	361	80.0	134	150	16.3	2.74	0.69	128	28.9	94.2	4.37	3.04	114
LA-21	Hbl	69.3	389	96.9	134	133	16.8	2.41	1.15	139	43.4	110	6.54	3.14	155
LA-22	Hbl	61.3	351	95.5	129	123	17.4	2.88	1.19	84.8	45.5	84.7	5.51	2.23	68.6
LA-24	Hbl	46.2	360	88.0	141	151	16.3	2.30	1.00	123	28.2	96.6	3.65	1.92	114
LA-25	Hbl	22.9	303	76.0	132	152	13.4	2.00	0.72	92.5	19.2	78.4	2.87	2.30	73.9
LA-26	Hbl	85.5	336	74.5	113	118	15.4	2.88	0.79	93.8	48.1	74.0	5.57	3.10	83.7
LA-23	Hbl	92.8	256	48.8	114	150	10.9	2.47	0.39	44.7	45.7	39.8	3.08	2.28	67.1
LA-4	Bt	5.54	1887	420	14.5	90.9	45.0	1.50	268	3.76	–	0.42	6.17	3.75	3997
LA-5	Bt	5.16	1684	531	14.0	89.8	44.6	1.11	273	2.92	–	0.42	5.55	2.94	3098
LA-6	Bt	5.49	1565	854	14.7	89.8	45.4	1.56	305	3.04	–	0.62	6.03	3.53	2808
LA-18	Bt	12.4	1836	266	24.6	95.9	42.2	0.89	269	3.60	–	0.73	6.96	4.32	5812
LA-19	Bt	13.5	1904	806	18.0	89.8	43.2	1.84	308	2.42	–	0.72	6.36	4.08	3459
LA-20	Bt	12.0	2011	696	21.4	91.0	44.9	0.96	295	2.67	–	0.73	6.17	2.52	4703
LA-27	Bt	11.1	1406	117	41.3	107	45.2	1.71	301	3.27	–	0.86	7.74	2.78	2975
LA-28	Bt	8.44	1095	254	25.9	108	44.9	1.33	334	2.78	–	0.87	8.69	2.58	1995
LA-29	Bt	8.56	1146	283	27.8	105	45.1	1.70	312	4.36	–	1.07	9.79	3.44	2124
LA-30	Bt	11.8	808	168	63.9	122	41.1	1.72	277	3.63	–	1.05	6.73	3.27	3036
BCK2-1 granodiorite porphyry															
LA-8	Bt	12.1	489	151	135	123	36.4	1.69	262	13.8	–	4.25	17.1	4.23	5251
LA-9	Bt	13.2	491	111	97.4	140	43.1	2.02	230	11.7	–	2.62	15.3	3.42	5157
LA-10	Bt	24.1	745	185	55.1	71.7	45.4	2.11	280	7.90	–	1.17	14.6	5.55	7297
LA-11	Bt	10.4	481	93.7	137	147	34.8	1.82	234	17.5	–	4.16	12.5	3.71	7351
LA-13	Bt	11.6	481	108	130	128	36.4	1.06	239	15.6	–	4.10	14.3	3.99	7705
LA-12	Bt	18.1	520	112	107	90.4	42.4	2.14	251	9.63	–	2.67	16.4	4.18	6514
LA-2	Bt	12.4	476	138	137	91.7	37.8	1.67	251	13.3	–	3.97	16.9	4.20	6476
LA-4	Bt	12.2	504	153	115	80.8	40.3	2.18	266	8.80	–	2.90	16.9	5.13	5540
LA-1	Bt	11.2	483	122	126	86.8	37.3	1.39	248	11.7	–	3.85	16.4	3.86	8145
LA-3	Bt	11.6	491	123	117	90.8	38.2	2.17	257	10.4	–	3.22	15.9	5.08	7577
ZK213-218 hornblende diorite porphyry															
LA-4	Tsch	80.6	547	129	204	55.5	16.7	1.33	0.69	384	16.7	23.4	0.58	1.79	78.1
LA-5	Tsch	90.8	555	647	357	45.7	15.9	1.41	0.40	374	14.5	18.2	0.41	2.57	71.2
LA-6	Tsch	85.3	501	287	884	38.0	16.2	1.56	0.65	362	15.1	16.6	0.29	2.14	70.4
LA-8	Tsch	54.8	500	209	161	57.1	17.4	1.58	0.67	406	15.1	18.1	0.43	2.44	80.8
LA-9	Tsch	86.8	550	237	388	46.3	15.4	1.31	0.81	422	12.7	14.1	0.37	2.14	73.9
LA-10	Tsch	76.5	539	240	248	51.8	16.9	1.14	0.59	404	15.3	17.8	0.45	2.57	77.6
LA-11	Tsch	89.9	555	345	383	44.7	16.3	1.44	0.73	410	13.5	15.5	0.40	2.95	82.0
LA-12	Tsch	89.4	554	186	378	45.7	15.8	1.13	0.56	420	14.1	13.8	0.31	2.86	76.1
LA-2	Pl	1.19	0.84	1.70	0.00	5.59	23.3	0.00	1.50	2119	0.17	0.28	–	0.86	167
LA-14	Kfs	1.31	0.04	0.60	0.00	0.92	11.2	0.99	151	536	0.27	21.5	0.05	1.94	1430
LA-3	Kfs	1.13	0.00	0.97	1.77	0.79	10.5	1.16	470	641	–	1.73	–	3.88	3356
LA-13	Kfs	1.19	0.51	0.00	0.00	0.35	5.08	0.57	673	473	0.99	24.1	–	4.29	2376

Spot	Min.	La	Ce	Pr	Nd	Sm	Eu	Gd	Tb	Dy	Ho	Er	Tm	Yb	Lu	Ta
ZK209-284 diorite																
LA-1	Hbl	15.0	52.9	8.8	40.8	9.56	2.31	6.72	0.88	5.33	1.03	3.02	0.40	2.86	0.46	0.22
LA-2	Hbl	14.9	51.7	8.26	36.1	8.18	2.18	6.27	0.86	5.12	0.95	2.88	0.38	1.96	0.32	0.22
LA-3	Hbl	19.5	72.9	13.0	60.2	14.4	3.15	12.47	1.84	9.40	1.83	4.96	0.74	4.01	0.61	0.33
LA-7	Hbl	17.0	59.9	10.1	43.9	10.1	2.45	7.04	1.02	6.26	1.01	3.23	0.43	2.59	0.41	0.22
LA-21	Hbl	19.2	72.1	12.3	59.0	14.0	2.87	10.81	1.55	8.39	1.63	4.39	0.71	3.82	0.58	0.34
LA-22	Hbl	16.1	60.7	10.6	51.6	13.3	2.70	10.49	1.60	8.86	1.61	4.88	0.63	4.36	0.58	0.27
LA-24	Hbl	16.7	58.5	9.64	43.4	10.8	2.39	7.21	1.03	5.35	1.12	3.10	0.40	3.08	0.41	0.23
LA-25	Hbl	12.1	42.8	6.98	31.1	6.59	1.60	4.63	0.67	3.77	0.76	2.11	0.31	2.13	0.30	0.18
LA-26	Hbl	16.2	62.4	11.2	52.8	13.9	2.91	11.83	1.66	9.67	1.81	5.36	0.69	4.15	0.56	0.27
LA-23	Hbl	10.4	40.6	7.7	39.3	12.0	2.08	11.56	1.65	8.80	1.69	5.31	0.64	4.03	0.48	0.16
LA-4	Bt	–	–	–	–	–	–	–	–	–	–	–	–	–	–	0.32
LA-5	Bt	–	–	–	–	–	–	–	–	–	–	–	–	–	–	0.25
LA-6	Bt	–	–	–	–	–	–	–	–	–	–	–	–	–	–	0.42
LA-18	Bt	–	–	–	–	–	–	–	–	–	–	–	–	–	–	0.35
LA-19	Bt	–	–	–	–	–	–	–	–	–	–	–	–	–	–	0.29
LA-20	Bt	–	–	–	–	–	–	–	–	–	–	–	–	–	–	0.35
LA-27	Bt	–	–	–	–	–	–	–	–	–	–	–	–	–	–	0.48
LA-28	Bt	–	–	–	–	–	–	–	–	–	–	–	–	–	–	0.37
LA-29	Bt	–	–	–	–	–	–	–	–	–	–	–	–	–	–	0.57
LA-30	Bt	–	–	–	–	–	–	–	–	–	–	–	–	–	–	0.27
BCK2-1 granodiorite porphyry																
LA-8	Bt	–	–	–	–	–	–	–	–	–	–	–	–	–	–	0.55
LA-9	Bt	–	–	–	–	–	–	–	–	–	–	–	–	–	–	0.47
LA-10	Bt	–	–	–	–	–	–	–	–	–	–	–	–	–	–	0.41
LA-11	Bt	–	–	–	–	–	–	–	–	–	–	–	–	–	–	0.37

Table 3 (*continued*)

Spot	Min.	La	Ce	Pr	Nd	Sm	Eu	Gd	Tb	Dy	Ho	Er	Tm	Yb	Lu	Ta
LA-13	Bt	–	–	–	–	–	–	–	–	–	–	–	–	–	–	0.46
LA-12	Bt	–	–	–	–	–	–	–	–	–	–	–	–	–	–	0.44
LA-2	Bt	–	–	–	–	–	–	–	–	–	–	–	–	–	–	0.59
LA-4	Bt	–	–	–	–	–	–	–	–	–	–	–	–	–	–	0.55
LA-1	Bt	–	–	–	–	–	–	–	–	–	–	–	–	–	–	0.45
LA-3	Bt	–	–	–	–	–	–	–	–	–	–	–	–	–	–	0.43
ZK213-218 hornblende diorite porphyry																
LA-4	Tsch	1.19	5.62	1.15	7.59	2.92	1.17	3.76	0.56	3.58	0.73	2.13	0.23	1.27	0.18	–
LA-5	Tsch	0.82	3.69	0.87	6.56	2.35	0.85	2.96	0.41	2.70	0.52	1.64	0.16	1.06	0.16	–
LA-6	Tsch	0.87	4.06	0.97	6.01	2.54	0.72	3.30	0.40	3.08	0.58	1.81	0.21	1.05	0.18	–
LA-8	Tsch	1.00	4.21	0.88	5.99	3.00	0.81	2.66	0.46	2.69	0.50	1.88	0.19	1.21	0.20	–
LA-9	Tsch	0.76	3.25	0.77	5.54	2.10	1.00	2.78	0.45	3.04	0.53	1.45	0.17	1.00	0.18	–
LA-10	Tsch	0.94	4.23	0.93	6.46	2.34	1.12	3.33	0.44	3.30	0.61	1.34	0.25	1.44	0.18	–
LA-11	Tsch	0.86	3.69	0.92	5.49	2.24	1.16	2.77	0.48	2.94	0.49	1.23	0.23	0.89	0.16	–
LA-12	Tsch	0.71	3.63	0.80	5.95	1.83	0.87	2.81	0.50	2.44	0.47	1.52	0.19	1.21	0.14	–
LA-2	Pl	1.04	2.27	0.20	0.85	0.03	0.29	0.06	–	0.07	–	0.09	–	0.05	–	–
LA-14	Kfs	0.18	0.16	0.01	0.08	–	0.09	–	–	0.03	0.02	–	0.02	0.07	0.03	–
LA-3	Kfs	0.58	0.59	0.02	0.07	0.05	0.13	–	–	–	–	–	–	–	–	–
LA-13	Kfs	0.05	0.04	–	0.02	0.05	0.07	0.11	0.01	0.08	0.03	0.16	0.04	0.23	0.06	–

– represents contents below detection limit. Abbreviations: Bt, biotite; Hbl, Mg-hornblende; Kfs, K-feldspar; Min., mineral; Pl, plagioclase; Tsch, tschermakite.

Table 4
In situ zircon trace element compositions (in ppm) determined by LA-ICPMS from the Baogutu deposit.

Lithology	D						FGD		DP		GDP		HDP	
Sample	ZK003-233		BHS		BTC196		BXS		BSB		BCK2-1		BJSB	
n	17		18		19		23		13		15		10	
spot	Mean	1σ	Mean	1σ	Mean	1σ	Mean	1σ	Mean	1σ	Mean	1σ	Mean	1σ
P	385	96.9	287	83.9	359	106	323	54.6	342	145	242	56.7	337	61.8
Ti	17.0	4.65	11.8	3.49	13.0	5.12	20.6	6.51	8.2	4.06	8.6	1.85	11.0	5.34
Y	1357	421	1494	609	1724	808	1372	358	911	271	840	229	960	173
Nb	0.63	0.41	0.71	0.43	0.66	0.31	0.35	0.09	0.66	0.19	0.54	0.15	0.38	0.17
La	0.10	0.06	0.15	0.15	0.08	0.07	0.06	0.06	0.03	0.02	0.04	0.03	0.11	0.15
Ce	13.7	6.07	17.1	6.78	15.5	5.63	9.60	2.46	11.1	4.24	8.93	2.53	10.3	4.22
Pr	0.20	0.14	0.22	0.23	0.23	0.10	0.22	0.06	0.17	0.17	0.07	0.04	0.14	0.08
Nd	2.84	1.59	3.10	2.16	3.83	1.66	3.42	0.84	1.82	1.11	1.40	0.74	1.91	0.79
Sm	5.41	2.84	5.05	3.00	7.47	3.55	6.09	1.49	2.94	1.11	2.73	1.27	3.89	1.42
Eu	1.41	0.52	1.98	1.14	2.10	0.97	1.11	0.24	0.93	0.30	0.90	0.37	1.03	0.29
Gd	28.9	13.7	27.2	16.2	40.4	21.7	32.3	9.00	16.0	6.14	15.1	5.85	19.7	5.31
Tb	9.58	4.21	9.12	4.94	12.9	6.92	10.6	2.95	5.46	1.91	5.15	1.85	6.49	1.60
Dy	115	45.7	114	55.7	152	80.5	125	36.1	69.0	22.8	65.0	21.2	77.5	16.6
Ho	44.2	15.9	45.8	20.9	56.5	28.1	46.5	13.7	27.9	8.7	26.5	7.8	30.2	6.0
Er	202	63.4	224	94.7	250	115	202	58.0	136	39.8	129	34.1	140	24.8
Tm	43.0	11.6	50.9	20.0	51.5	21.0	40.5	11.0	31.2	8.76	29.7	6.77	30.2	4.90
Yb	412	97.6	525	195	482	173	363	93.2	318	88.1	303	62.8	296	51.1
Lu	83.1	16.5	114	40.1	96.5	30.4	67.4	16.6	67.8	18.5	64.8	12.6	61.2	12.3
Hf	7778	705	7481	366	8816	518	7685	408	8389	688	8494	379	8706	357
Ta	0.28	0.12	0.28	0.10	0.28	0.09	0.20	0.04	0.29	0.08	0.25	0.05	0.19	0.04
Pb	9.63	4.68	12.14	6.26	12.26	4.24	9.33	4.52	9.54	4.35	7.10	1.37	7.73	6.44
Th	115	75.6	177	101	164	83.3	117	66.9	87.7	40.4	61.3	20.4	81.8	72.5
U	134	60.4	165	81.3	163	54.6	133	61.8	143	64.3	111	20.8	108	86.8
T1 (°C)	787	29.3	752	27.5	758	41.4	805	30.3	716	44.0	726	20.0	738	53.8
T2 (°C)	795	31.4	758	29.5	764	44.3	815	32.7	719	46.8	730	21.3	743	57.3
Tave (°C)	791	30.4	755	28.5	761	42.8	810	31.5	717	45.4	728	20.7	741	55.5
$(Ce/Ce^*)_D$	28.1	9.3	36.0	11.3	35.6	12.6	26.0	11.4	48.8	17.8	46.0	10.9	33.1	13.7
$(Eu/Eu^*)_D$	0.39	0.12	0.52	0.03	0.40	0.05	0.24	0.03	0.45	0.07	0.36	0.06	0.36	0.10
log(fO_2) (Ce)	−13.6	1.2	−14.4	1.8	−14.3	2.1	−13.2	1.3	−15.3	2.0	−14.8	1.6	−14.1	1.7
ΔNNO (Ce)	0.6	0.9	0.6	1.4	0.6	1.5	0.5	1.4	0.6	1.2	0.8	1.2	0.5	1.7
ΔNNO (Eu)	1.9	1.5	3.6	0.4	2.0	0.7	−0.2	0.5	2.7	0.9	1.5	0.8	1.4	1.3

T1 and T2 are calculated according to Watson et al. (2006) and Ferry and Watson (2007). The $(Ce/Ce^*)D$, $(Eu/Eu^*)D$, log(fO2) (Ce), ΔNNO (Ce) and ΔNNO (Eu) are calculated according to Trail et al. (2012). Abbreviations: D, diorite; FGD, fine grained diorite; DP, diorite porphyry; GDP, granodiorite porphyry; HDP, hornblende diorite porphyry.

showed that the mineral/melt (or rock) distribution for isovalent cations is a function of the ionic radius, and demonstrated that correlations could be described by concave-down parabolic curves (Fig. 10a). Blundy and Wood (1994) quantified this relationship using a lattice strain model which can be used to predict elemental partitioning behavior. Based on this model, Ballard et al. (2002) noted a linear relationship fitted by a straight line between zircon/melt distribution coefficients (D_i) for the REEs and a lattice strain term involving their ionic radii (r_i):

$$\ln D_i = \ln D_0 - (4\pi E N_A/RT) * (r_i/3 + r_0/6) * (r_i - r_0)^2$$

where D_0 is the strain-free distribution coefficient, E is the Young's modulus, N_A is the Avogadro number, R is the gas constant, T is the

Table 5
In situ apatite trace element compositions (in ppm) determined by LA-ICPMS from the Baogutu deposite.

Spot	Na	Mg	V	Mn	Fe	Ga	Ge	Rb	Sr	Y	Zr	Sn	Ba	La	Ce	Pr	Nd	Sm
diorite ZK003-233																		
LA-01	363	25.6	25.1	220	549	19.6	5.89	0.18	252	549	0.81	1.22	0.83	723	1601	203	866	148
LA-02	768	38.9	29.2	295	486	30.7	10.9	0.43	312	493	0.81	1.61	1.68	982	2258	274	1146	197
LA-03	360	20.4	15.8	181	394	19.7	5.76	0.06	225	548	0.44	1.39	0.59	770	1760	216	873	151
LA-04	496	169	14.3	251	621	32.7	11.7	0.41	231	566	0.89	1.57	1.37	1068	2348	286	1219	203
LA-05	507	16.3	29.1	182	1208	21.6	8.63	0.19	305	364	0.57	1.51	0.55	621	1397	298	1197	209
LA-06	804	51.3	20.1	364	532	22.8	7.42	0.07	345	608	0.72	1.39	0.47	884	2063	243	1018	169
LA-07	762	50.7	31.9	296	551	22.9	7.60	0.06	276	505	1.24	1.61	0.57	942	2084	247	1031	164
LA-08	523	17.4	10.4	198	259	20.7	7.13	0.08	266	396	0.28	1.68	0.49	747	1646	208	848	150
LA-09	404	37.3	12.4	235	389	15.9	5.31	0.08	231	424	0.22	1.73	0.45	637	1356	160	701	113
LA-10	543	31.1	26.5	245	549	22.9	7.24	0.15	303	315	0.96	1.41	0.62	838	1859	224	1000	160
LA-11	876	38.6	22.7	278	611	29.8	8.98	0.15	321	495	1.46	1.60	5.47	1183	2655	328	1378	224
LA-12	808	61.0	32.6	339	529	23.8	7.61	0.36	240	730	0.71	1.16	1.41	881	2041	241	1041	165
LA-13	493	26.7	19.5	211	490	22.2	7.33	0.11	271	368	1.22	1.27	0.56	750	1722	213	849	142
LA-14	501	50.2	18.4	271	374	25.4	7.90	0.24	251	360	1.13	1.60	0.82	954	2160	266	1116	185
LA-15	913	229	32.8	379	743	25.2	7.48	0.35	359	425	1.70	1.31	0.45	926	2099	253	1086	180
LA-16	475	130	35.3	244	1061	20.9	14.5	0.78	229	328	0.75	1.28	1.46	746	1629	194	806	131
LA-17	354	15.7	12.9	167	309	15.3	5.02	0.15	261	369	0.51	1.07	0.70	765	1701	205	861	141
LA-18	849	45.6	40.2	328	416	27.2	8.31	0.07	291	422	1.04	1.35	0.58	1028	2256	271	1142	180
LA-19	956	72.2	2.65	312	691	6.55	1.68	0.66	249	414	0.57	1.53	0.48	776	1712	214	872	148
LA-20	414	35.1	19.4	247	459	18.0	5.91	0.01	203	442	0.51	0.92	0.27	706	1547	187	797	129
granodiorite porphyry BCK2-1																		
LA-01	750	117	15.4	573	895	21.7	8.64	0.38	519	377	0.30	1.11	3.44	626	1396	160	713	134
LA-02	427	83.3	8.28	401	589	19.7	8.30	0.51	379	398	0.82	1.45	1.27	545	1192	145	676	136
LA-03	777	160	11.1	786	987	24.9	10.1	0.13	562	433	0.99	1.12	3.91	763	1682	184	823	156
LA-04	536	158	19.3	396	655	19.3	8.73	0.06	433	460	1.05	1.21	1.97	557	1213	151	710	150
LA-05	488	280	35.4	1056	1754	30.8	12.2	0.22	575	522	0.68	1.29	3.97	924	2043	220	984	188
LA-06	566	306	8.22	1144	1847	31.8	12.8	0.17	594	572	1.74	1.05	4.94	1001	2211	241	1090	207
LA-07	419	122	11.2	621	857	30.7	11.8	0.18	513	562	1.66	1.29	2.46	929	2068	229	1045	200
LA-08	484	217	5.04	893	1789	27.7	11.2	0.05	585	486	0.62	1.05	3.95	867	1838	208	931	176
LA-09	721	76.5	23.8	408	711	24.7	10.3	0.51	452	457	0.73	1.02	4.55	715	1631	184	840	159
LA-10	498	164	2.98	734	1063	26.9	11.2	0.17	505	476	0.43	1.13	3.12	804	1766	195	896	172
LA-11	1043	243	37.9	1102	1534	28.7	11.2	0.07	603	495	1.45	1.35	5.30	874	1941	212	965	183
LA-12	422	220	12.7	360	912	26.5	11.7	0.49	384	543	1.04	1.23	1.52	765	1718	198	935	182
LA-13	599	121	12.2	419	602	26.6	11.0	0.95	477	519	0.82	1.04	2.40	802	1806	199	935	179
LA-14	849	92.5	19.9	385	566	23.6	9.59	0.27	398	488	1.04	1.05	1.78	655	1564	175	824	160
LA-15	477	168	29.5	607	1969	30.6	12.4	0.68	514	578	1.15	1.19	3.07	840	2082	229	1070	204
LA-16	485	267	15.2	513	800	27.1	11.7	0.33	455	504	1.81	1.13	3.04	790	1753	195	897	173
LA-17	570	170	59.4	697	955	27.6	11.3	0.15	529	508	0.91	1.28	4.37	827	1851	204	919	178
LA-18	554	249	8.88	897	1272	27.7	11.5	0.10	545	502	2.21	1.42	4.59	847	1856	203	929	177
LA-19	806	91.6	42.1	387	607	27.2	10.9	0.13	423	584	0.59	1.68	2.17	735	1689	206	954	192
LA-20	544	199	36.0	576	995	23.5	9.33	0.48	501	485	1.22	1.12	3.35	614	1411	179	812	158
hornblende diorite porphyry ZK213-218																		
LA-01	537	80.5	10.8	900	399	14.7	5.47	0.14	201	253	1.61	1.54	1.67	377	896	100	358	59.7
LA-02	351	51.8	4.16	304	322	22.8	7.73	0.61	185	427	0.80	1.02	0.91	659	1584	174	639	112
LA-03	268	68.7	9.28	368	1712	8.54	2.89	0.18	179	197	0.81	1.27	0.98	205	490	62.5	237	37.4
LA-04	67.5	60.3	25.3	356	514	24.2	6.15	0.44	220	255	0.31	1.44	0.54	921	2172	228	887	145
LA-05	822	67.4	31.7	903	1797	22.0	6.38	0.14	184	324	2.12	1.10	2.19	781	1842	201	752	127
LA-06	393	74.7	7.11	422	246	11.1	4.83	0.06	205	152	0.61	0.93	0.58	273	654	72.8	283	51.3
LA-07	205	61.9	8.31	380	862	5.40	2.03	0.27	206	199	0.58	0.88	0.62	101	250	27.2	112	22.7
LA-08	202	147	5.37	446	767	3.51	1.42	0.18	240	224	0.20	1.43	0.48	852	2030	235	841	148
LA-09	77.9	46.0	2.83	218	205	3.01	1.00	0.11	275	119	0.62	1.36	0.22	561	1395	124	455	75.9
LA-10	294	264	8.08	459	507	8.18	3.46	0.20	184	282	0.68	1.25	0.14	190	470	54.4	194	32.7
LA-11	114	39.0	2.81	332	186	1.50	0.83	0.09	179	442	0.10	1.37	0.47	473	1123	123	463	78.9
LA-12	247	198	8.55	425	565	8.88	3.67	0.12	237	234	0.76	1.56	0.75	231	549	65.3	237	37.2
LA-13	321	56.1	20.9	399	913	5.21	1.85	0.76	252	158	0.28	1.70	1.24	473	1167	127	451	78.2
LA-14	783	59.0	30.4	885	1526	19.6	5.75	0.11	272	333	2.48	1.04	1.87	711	1656	175	678	116
LA-15	323	146	10.0	309	377	4.03	1.57	0.15	210	123	1.09	1.63	2.70	150	366	41.1	162	25.2

Spot	Eu	Gd	Tb	Dy	Ho	Er	Tm	Yb	Lu	Pb	Th	U	REE	Eu*	$\log fO_2^{\dagger}$	$\Delta NNO^{\ddagger}$
diorite ZK003-233																
LA-01	20.1	119	13.4	63.5	12.3	30.2	3.60	23.2	3.50	0.92	9.73	7.51	3830	0.46	−10.2	3.3
LA-02	19.1	150	18.5	94.5	17.5	42.7	5.33	33.5	4.37	1.60	18.2	10.7	5242	0.34	−10.4	3.2
LA-03	15.2	117	14.6	76.3	14.5	35.4	4.30	26.2	3.89	0.55	11.7	6.76	4077	0.35	−10.1	3.4
LA-04	19.5	146	21.0	101	19.8	48.1	5.83	35.1	4.71	2.27	47.8	4.53	5526	0.35	−10.3	3.3
LA-05	22.8	157	21.2	99.1	18.6	45.2	5.72	35.3	5.04	0.93	17.4	12.4	4133	0.38	−10.2	3.4
LA-06	17.6	129	17.5	98.3	17.6	42.8	5.73	30.2	4.08	0.82	9.02	3.55	4741	0.36	−10.6	3.0
LA-07	17.2	121	16.0	85.0	15.1	36.1	4.59	27.8	3.61	0.92	8.21	3.12	4794	0.37	−10.4	3.2
LA-08	12.8	105	14.9	71.8	14.4	31.2	4.08	26.2	3.58	0.39	9.20	6.28	3883	0.31	−10.2	3.4
LA-09	10.2	76.2	9.82	51.1	11.0	25.0	2.70	18.5	2.72	0.64	7.61	4.36	3174	0.33	−10.3	3.3
LA-10	15.8	113	15.6	74.8	15.8	34.8	4.72	25.0	3.94	0.89	10.7	7.56	4385	0.36	−10.3	3.3
LA-11	22.7	157	21.3	109	20.6	49.1	6.49	36.6	5.40	2.46	13.6	4.54	6196	0.37	−10.4	3.2
LA-12	16.2	122	17.3	86.0	16.9	39.5	4.64	30.6	3.86	1.37	16.7	6.18	4705	0.35	−10.5	3.1

Table 5 (*continued*)

Spot	Eu	Gd	Tb	Dy	Ho	Er	Tm	Yb	Lu	Pb	Th	U	REE	Eu*	log$fO_2^\downarrow$	ΔNNO‡
LA-13	13.9	115	15.7	77.3	14.1	37.0	4.88	23.4	3.77	1.03	14.3	10.3	3983	0.33	−10.2	3.4
LA-14	18.3	132	18.9	93.2	18.9	45.1	5.32	31.8	4.39	1.05	21.2	8.46	5047	0.36	−10.3	3.2
LA-15	17.1	127	17.4	89.2	16.9	43.4	4.79	31.1	4.00	1.58	7.75	2.86	4895	0.35	−10.6	3.0
LA-16	12.9	92.2	12.4	62.7	11.9	29.6	3.65	21.6	2.82	0.61	8.76	5.18	3755	0.36	−10.3	3.3
LA-17	15.6	109	13.5	70.3	14.8	34.8	4.26	25.5	3.50	1.21	8.52	6.50	3964	0.39	−10.1	3.5
LA-18	17.9	132	16.7	87.9	16.9	40.7	4.96	30.5	3.89	0.76	12.3	4.14	5228	0.36	−10.5	3.1
LA-19	14.3	108	15.5	71.9	13.2	33.5	4.37	26.5	3.39	6.91	6.61	4.59	4013	0.34	−10.4	3.1
LA-20	13.0	103	13.6	71.5	13.4	30.9	3.83	23.4	3.04	0.70	12.1	8.63	3642	0.34	−10.3	3.3
granodiorite porphyry BCK2-1																
LA-01	14.7	111	14.3	68.4	13.1	33.9	3.78	22.5	3.21	1.67	7.06	2.43	3315	0.37	−11.0	2.6
LA-02	13.6	116	15.0	71.1	13.5	35.8	4.02	23.9	3.62	1.41	15.0	3.42	2991	0.33	−10.6	2.9
LA-03	17.4	126	16.7	78.4	14.7	38.2	4.43	24.8	3.64	2.01	11.8	3.61	3931	0.38	−11.5	2.1
LA-04	18.6	135	17.5	81.0	16.1	41.6	4.83	27.8	4.12	1.33	11.2	3.39	3129	0.40	−10.6	3.0
LA-05	20.4	150	20.1	93.1	18.0	45.8	5.27	29.8	4.30	2.53	11.5	4.02	4746	0.37	−12.1	1.5
LA-06	23.0	167	21.8	102	19.8	50.6	5.99	33.4	4.69	2.68	14.5	4.13	5181	0.38	−12.3	1.3
LA-07	20.3	163	21.0	100	19.4	49.7	5.96	33.0	4.74	1.81	17.2	5.10	4890	0.34	−11.1	2.5
LA-08	19.9	143	18.6	87.2	16.9	42.3	4.95	27.8	4.05	2.11	12.8	4.09	4386	0.38	−11.7	1.9
LA-09	15.9	134	17.1	81.9	15.9	40.4	4.62	26.4	3.70	1.89	15.5	4.25	3868	0.33	−10.6	2.9
LA-10	17.4	137	18.0	85.8	16.4	41.6	5.03	26.9	4.25	1.76	11.4	4.35	4185	0.35	−11.4	2.2
LA-11	20.6	144	18.8	89.8	17.2	43.6	5.06	29.4	4.15	2.53	13.8	3.97	4546	0.39	−12.2	1.4
LA-12	17.1	153	20.3	98.6	19.0	48.6	5.82	33.9	4.67	3.00	20.5	5.14	4198	0.31	−10.5	3.0
LA-13	18.1	148	19.7	93.3	18.0	46.7	5.44	30.8	4.47	1.80	15.7	4.78	4305	0.34	−10.7	2.9
LA-14	16.4	130	17.7	84.4	17.0	44.1	5.08	30.6	4.50	1.05	11.6	3.53	3728	0.35	−10.6	3.0
LA-15	21.5	162	21.5	104	19.7	51.0	6.12	34.0	4.91	1.89	13.4	3.78	4850	0.36	−11.1	2.5
LA-16	17.3	141	18.8	88.1	17.3	44.8	5.21	30.3	4.26	1.76	14.5	4.58	4174	0.34	−10.9	2.7
LA-17	19.2	144	19.1	90.2	17.4	45.2	5.19	31.1	4.22	3.05	13.1	4.12	4356	0.37	−11.3	2.3
LA-18	19.3	140	18.8	87.9	17.3	43.8	5.34	30.9	4.34	2.53	14.0	4.02	4380	0.37	−11.7	1.9
LA-19	19.0	155	21.1	100	19.9	51.9	6.15	36.6	5.41	3.07	19.3	5.58	4192	0.34	−10.6	3.0
LA-20	16.8	131	17.7	86.0	16.6	43.0	5.09	29.4	4.10	1.63	6.56	2.68	3523	0.36	−11.0	2.6
hornblende diorite porphyry ZK213-218																
LA-01	5.42	40.3	4.82	28.9	4.9	15.7	1.85	12.6	1.94	6.58	41.4	11.8	1908	0.34	−11.7	1.9
LA-02	10.1	71.1	8.65	48.0	8.6	26.7	2.94	21.8	3.17	1.06	23.8	3.71	3369	0.35	−10.4	3.2
LA-03	3.45	25.5	3.14	18.6	3.4	9.79	1.33	6.85	1.25	3.07	4.28	0.77	1105	0.34	−10.6	3.0
LA-04	12.6	95.7	11.1	64.4	11.4	34.0	3.95	27.2	4.06	1.83	72.8	0.84	4617	0.33	−10.5	3.0
LA-05	11.4	82.0	9.87	55.4	10.0	30.6	3.64	24.4	3.70	3.11	52.9	0.51	3934	0.34	−11.7	1.8
LA-06	3.96	29.6	3.46	21.4	3.58	10.5	1.56	8.91	1.45	0.40	1.36	0.37	1418	0.31	−10.7	2.9
LA-07	1.89	13.7	1.56	8.56	1.46	4.77	0.75	3.56	0.74	0.32	3.11	0.57	550	0.33	−10.6	3.0
LA-08	13.2	92.2	10.7	66.1	11.8	33.4	3.94	28.5	4.02	1.35	2.05	0.15	4369	0.34	−10.7	2.8
LA-09	6.65	52.0	6.10	34.9	6.30	20.0	2.25	15.5	2.46	2.04	1.85	0.47	2757	0.32	−10.2	3.4
LA-10	2.83	21.6	2.61	14.5	2.82	7.53	0.95	6.40	1.10	0.39	3.89	0.51	1001	0.32	−10.8	2.8
LA-11	6.99	53.5	6.55	33.1	5.93	19.5	2.30	15.1	2.31	0.42	1.75	0.10	2406	0.33	−10.5	3.1
LA-12	3.61	26.5	3.17	20.0	3.29	9.76	1.25	7.97	1.29	0.86	8.35	0.69	1197	0.35	−10.7	2.9
LA-13	7.06	56.5	6.04	35.7	6.15	19.4	2.38	15.7	2.51	0.37	2.27	0.20	2448	0.32	−10.6	3.0
LA-14	10.2	75.5	8.79	52.0	8.97	27.4	3.03	22.6	3.28	3.16	42.3	2.16	3548	0.33	−11.7	1.9
LA-15	2.37	19.9	2.17	13.6	2.19	5.85	0.96	5.39	0.81	0.48	4.97	0.41	797	0.32	−10.4	3.1

$Eu^* = Eu_N/(Sm_N * Gd_N)0.5$. $\log fO_2^\downarrow = -0.0022 * Mn(ppm) - 9.75$ according to Miles et al. (2014). $\Delta NNO^\ddagger = \log fO_2$-NNO at 820 °C according to ~820 °C apatite saturation temperature and 2 kbar pressure from Cao et al. (2014a).

absolute temperature, r_0 is the optimal site radius (assumed to be 0.84 Å for Zr in eightfold coordination). The straight lines represent the parabolas described by Onuma et al. (1968). Ballard et al. (2002) showed that the scale of positive Ce anomalies relative to the straight line could be used to estimate the zircon Ce^{4+}/Ce^{3+} ratios and oxidation state of the magma. Figure 10b shows an obvious negative linear correlation between $\ln D_i$ and $(r_i/3 + r_{Zr}/6) * (r_i - r_{Zr})^2$ for almost all REEs except Eu and Ce, and similar positive Ce anomalies relative to the straight line, indicating similar oxidation states for all rocks.

Based on the results of Ballard et al. (2002), Trail et al. (2012) utilized the Ce and Eu anomalies of zircon/melt distribution coefficients (D_i) to estimate the oxygen fugacity as follows:

$$\ln(Ce/Ce^*)_D = \ln(D_{Ce}/(D_{La} * D_{Pr})^{0.5}) = (0.1156 + 0.0050) * \ln(fO_2) + (13860 \pm 708)/T(K) - 6.125 \pm 0.484$$

$$1/(Eu/Eu^*)_D = 1/(D_{Eu}/(D_{Sm} * D_{Gd})^{0.5}) = 1 + 10^{(-0.14\pm0.01*\Delta NNO+0.47\pm0.04)}$$

where $(Ce/Ce^*)_D$ and $(Eu/Eu^*)_D$ are Ce and Eu anomalies calculated from zircon/melt distribution coefficients, T is the zircon crystallization temperature calculated by Ti in zircon thermometry (after Watson et al., 2006; Ferry and Watson, 2007), and ΔNNO is the difference in log units from the NNO buffer at the corresponding zircon crystallization temperature.

Using the bulk rock REE concentrations (Cao et al., 2016a) to represent the melt contents, we calculated the ΔNNO values independently, according to Ce and Eu anomalies. The results calculated according to the Ce anomaly show consistent ΔNNO variations with a mean ΔNNO value of 0.6 ± 0.9 (1σ, n = 17) for the diorite ZK003-233, 0.6 ± 1.4 (1σ, n = 18) for the diorite BHS, 0.6 ± 1.5 (1σ, n = 19) for the diorite BTC196, 0.5 ± 1.4 (1σ, n = 23) for the fine-grained diorite BXS, 0.6 ± 1.2 (1σ, n = 13) for the diorite porphyry BSB, 0.8 ± 1.2 (1σ, n = 15) for the granodiorite porphyry BCK2-1, 0.5 ± 1.7 (1σ, n = 10) for the hornblende diorite porphyry BJSB (Fig 10c), which show similar values with that estimated on diorite by Shen et al. (2015). However, the ΔNNO values based on the Eu anomaly show significant variations from 3.6 ± 0.4 in BHS to −0.2 ± 0.5 in BXS (Fig. 10c).

Based on the results of this study and our previously published data (Cao et al., 2014c, 2015a), the K-feldspar, amphibole, apatite,

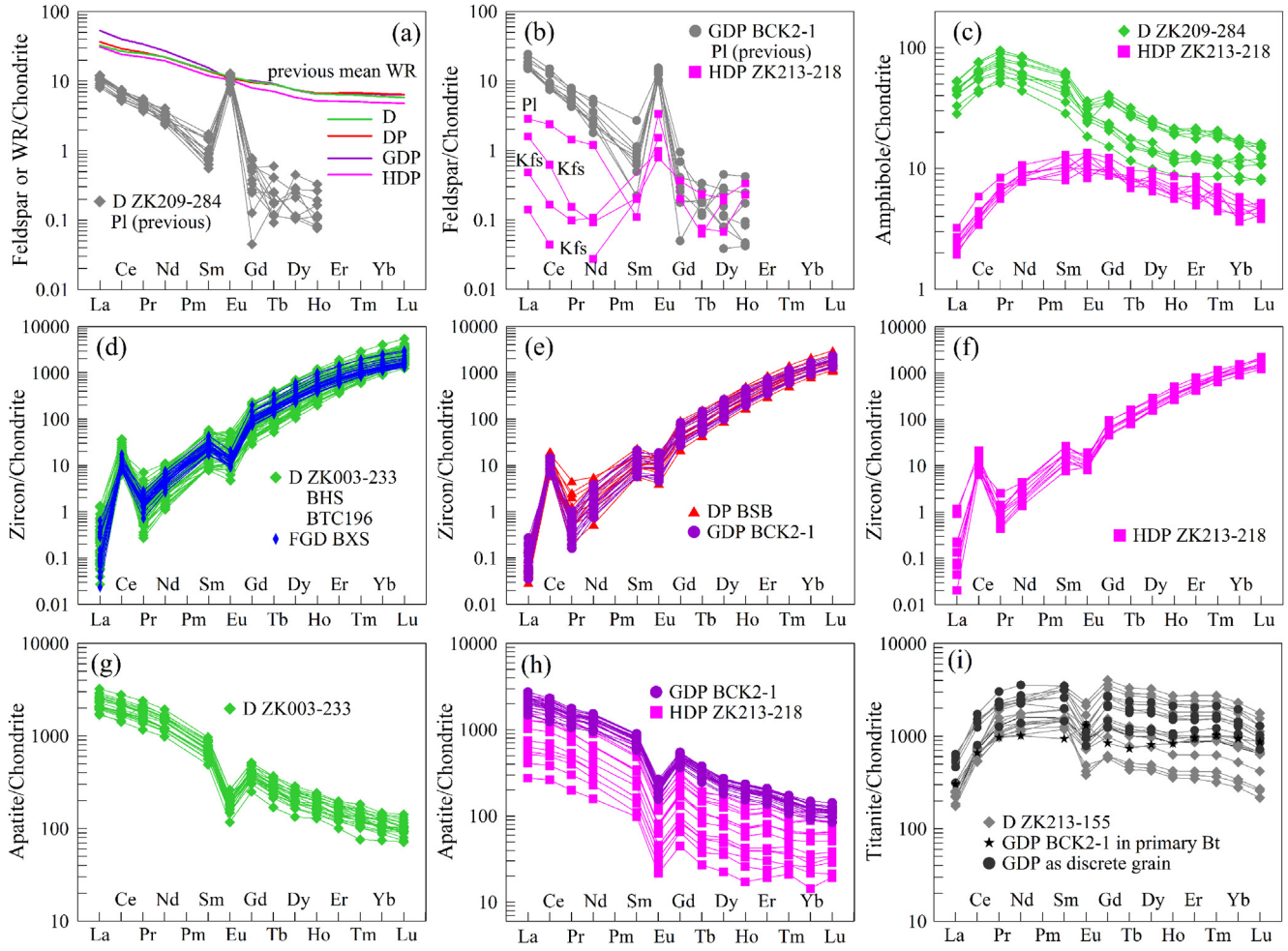

Fig. 6. Chondrite-normalized REE patterns of feldspar and mean whole rock (WR) (a, b), amphibole (c), zircon (d, e, f), apatite (g, h) and titanite (i) from the Baogutu deposit. Chondrite REE values are from Taylor and McLennan (1985). Previously published plagioclase, whole rock and titanite compositions are from Cao et al. (2014c, 2015a, 2016a).

plagioclase and titanite do not preferentially deplete or enrich Ce relative to neighboring La and Pr (Fig. 6), biotite does not incorporate significant REEs, similar to quartz and ilmenite/magnetite. Thus, the $(Ce/Ce^*)_D$ will not be affected by other mineral crystallization and may be the most stable indicator to constrain the fO_2 of magma (Trail et al., 2012). In contrast, plenty of mineral phases will influence Eu anomalies in the melt. Plagioclase preferentially incorporates Eu relative to Sm and Gd (Drake and Weill, 1975), consistent with obvious positive Eu anomalies in the chondrite-normalized REE patterns (Fig. 6). Thus, plagioclase crystallization will significantly deplete the melt in Eu relative to Sm and Gd and generate negative Eu anomalies in the later crystallized mineral phases. This is consistent with a slightly positive Eu anomaly in early crystallized titanite, occurring as inclusions within a primary biotite phenocryst, but an obvious negative Eu anomaly in later crystallized titanite in the matrix (Cao et al., 2015b). In addition, amphibole, apatite and titanite (Fig. 6) show consistently negative Eu anomalies which will influence the Eu content in the residual melt. If zircon is the first phase crystallized from the magma, the oxidation state calculated from $(Ce/Ce^*)_D$ and $(Eu/Eu^*)_D$ will be identical. On the contrary, if plagioclase, amphibole, apatite and titanite crystallize before or at the same time as zircon, the oxidation states from $(Ce/Ce^*)_D$ and $(Eu/Eu^*)_D$ in zircon will be different. Different ΔNNO values according to Ce and Eu anomaly (Fig. 10) suggest that zircon is not the first crystallizing phase, and that the Eu anomaly should not be used to constrain the oxidation state of magma at the Baogutu deposit.

5.2.2. Oxidation state of granitoids revealed by apatite

Due to the immobility of Mn in apatite after crystallization (Fig. 9), Mn in apatite could be used to estimate the fO_2 of granitoids as proposed by Miles et al. (2014) according to the following equation: $\log fO_2 = -0.0022(\pm0.0003)Mn(ppm) - 9.75(\pm0.46)$. If this works, results will be similar to those obtained using zircon. Our results show $\log fO_2$ values of −10.6 to −10.1 (mean = −10.3; 1σ = 0.1; n = 20) for ZK003-233 diorite, −12.3 to −10.5 (mean = −11.2; 1σ = 0.6; n = 20) for granodiorite porphyry BCK2-1, and −11.7 to −10.2 (mean = −10.8; 1σ = 0.5; n = 15) for hornblende diorite porphyry ZK213-218, corresponding to ΔNNO values of 3.3 ± 0.1, 2.4 ± 0.6 and 2.8 ± 0.5, respectively, at the apatite saturation temperature of ~820 °C (Cao et al., 2014a). The mean ΔNNO of 2.4 to 3.3 are obviously higher than the 0.5 to 0.8 estimated using the zircon Ce anomaly. In addition, the high fO_2 values in S-bearing magma (≥NNO + 1 after Parat and Holtz, 2005) require the occurrence of highly oxidized minerals (anhydrite, hematite), the absence of magmatic pyrrhotite and also high contents of SO_3 in apatite (>0.55 wt.%). However, none of the Baogutu granitoids contain magmatic hematite or anhydrite. They do contain abundant magmatic pyrrhotite and have relatively low contents of SO_3 in apatite, indicating a relatively low oxidation state (fO_2 less than NNO + 1) in the magma. It is consistent with fO_2 values of 0.5 to 0.8 estimated according to the zircon Ce anomaly but significantly lower than that estimated by Mn in apatite, which could also be explained by mineral crystallization.

Similar to the zircon Eu anomaly, Mn contents in apatite are also significantly affected by the crystallization of other minerals.

Table 6
In situ apatite Nd isotopic data determined by LA-MC-ICPMS from the Baogutu deposit.

Spot	wide (μm)	long (μm)	Size ave.(μm)	$^{147}Sm/^{144}Nd$ (2σ)	$^{143}Nd/^{144}Nd$ (2σ)	$^{145}Nd/^{144}Nd$ (2σ)	$(^{143}Nd/^{144}Nd)_i$	εNd(t)	2σ	T_{DM2}	$f_{Sm/Nd}$
diorite ZK003-233											
LA-01	85.3	120.5	102.9	0.1190(2)	0.51281(5)	0.34840(4)	0.51256	6.6	1.1	544	−0.39
LA-02	78.6	125.3	102.0	0.1113(7)	0.51279(4)	0.34842(2)	0.51256	6.5	0.8	547	−0.43
LA-03	100.2	140.5	120.4	0.1116(9)	0.51281(3)	0.34840(2)	0.51258	6.8	0.6	523	−0.43
LA-04	120.5	152.3	136.4	0.1029(7)	0.51280(4)	0.34841(3)	0.51259	7.1	0.9	504	−0.48
LA-05	95.3	130.5	112.9	0.1174(5)	0.51282(4)	0.34841(3)	0.51257	6.8	0.9	525	−0.40
LA-06	89.3	120.4	104.9	0.1129(2)	0.51281(5)	0.34842(3)	0.51257	6.8	0.9	527	−0.43
LA-07	105.3	130.5	117.9	0.1180(7)	0.51278(5)	0.34842(3)	0.51253	6.0	1.0	592	−0.40
LA-08	86.3	98.6	92.5	0.1232(9)	0.51280(5)	0.34842(3)	0.51254	6.2	1.0	577	−0.37
LA-09	82.3	120.5	101.4	0.1116(1)	0.51281(5)	0.34840(3)	0.51258	6.8	1.0	524	−0.43
LA-10	85.3	125.3	105.3	0.1189(8)	0.51282(5)	0.34842(3)	0.51257	6.7	0.9	535	−0.40
LA-11	110.5	153.6	132.1	0.1203(2)	0.51280(5)	0.34842(3)	0.51254	6.2	1.0	574	−0.39
LA-12	120.5	145.6	133.1	0.1095(6)	0.51281(4)	0.34840(3)	0.51258	7.0	0.7	514	−0.44
LA-13	135.5	160.5	148.0	0.1033(2)	0.51274(5)	0.34841(3)	0.51253	5.9	0.9	600	−0.47
LA-14	99.4	130.5	115.0	0.1033(1)	0.51275(6)	0.34841(4)	0.51254	6.1	1.1	586	−0.47
LA-15	115.2	140.7	128.0	0.1138(1)	0.51286(5)	0.34837(3)	0.51262	7.6	1.0	458	−0.42
LA-16	88.6	115.2	101.9	0.1136(1)	0.51280(4)	0.34839(3)	0.51256	6.6	0.8	544	−0.42
LA-17	94.3	130.7	112.5	0.1141(8)	0.51285(5)	0.34841(3)	0.51261	7.4	1.0	475	−0.42
LA-18	108.7	135.6	122.2	0.1057(6)	0.51283(5)	0.34840(3)	0.51261	7.6	1.0	464	−0.46
LA-19	118.6	130.5	124.6	0.1221(5)	0.51280(6)	0.34839(4)	0.51254	6.2	1.1	576	−0.38
LA-20	142.3	175.2	158.8	0.1135(6)	0.51284(5)	0.34840(2)	0.51260	7.3	0.9	482	−0.42
LA-21	125.5	145.8	135.7	0.1029(7)	0.51275(6)	0.34841(4)	0.51253	6.0	1.1	589	−0.48
LA-22	105.3	132.4	118.9	0.0974(1)	0.51277(6)	0.34842(3)	0.51257	6.7	1.2	536	−0.50
LA-23	134.5	165.7	150.1	0.1253(7)	0.51283(5)	0.34842(3)	0.51258	6.4	0.9	543	−0.36
LA-24	105.4	131.7	118.6	0.1075(2)	0.51279(5)	0.34841(3)	0.51257	6.3	1.1	549	−0.45
mean				0.1125	0.51280	0.34841	0.51257	6.7	0.9	537	-0.43
granodiorite porphyry BCK2-1											
LA-01	230.5	328.6	279.6	0.1054(7)	0.51278(3)	0.34840(2)	0.51257	6.4	0.6	553	−0.46
LA-02	166.6	232.9	199.8	0.1053(3)	0.51274(6)	0.34842(3)	0.51252	5.6	1.1	619	−0.46
LA-03	175.1	188.9	182.0	0.1044(9)	0.51278(5)	0.34841(4)	0.51257	6.5	1.1	543	−0.47
LA-04	163.2	185.1	174.2	0.1007(2)	0.51277(4)	0.34844(2)	0.51257	6.4	0.7	550	−0.49
LA-05	132.9	195.5	164.2	0.0974(1)	0.51278(2)	0.34839(2)	0.51258	6.7	0.4	527	−0.50
LA-06	167.3	179.8	173.6	0.1056(3)	0.51279(4)	0.34840(2)	0.51258	6.6	0.7	537	−0.46
LA-07	140.1	240.6	190.4	0.0992(9)	0.51273(2)	0.34842(2)	0.51253	5.6	0.4	613	−0.50
LA-08	127.1	188.3	157.7	0.1018(2)	0.51280(3)	0.34839(2)	0.51259	6.9	0.5	512	−0.48
LA-09	120.2	245	182.6	0.1023(2)	0.51279(3)	0.34840(2)	0.51258	6.7	0.5	528	−0.48
LA-10	102	173.8	137.9	0.1001(1)	0.51278(3)	0.34841(2)	0.51258	6.7	0.6	530	−0.49
LA-11	113.2	166.6	139.9	0.1100(3)	0.51282(5)	0.34841(3)	0.51259	6.9	1.0	507	−0.44
LA-12	121.1	209.1	165.1	0.0973(1)	0.51277(3)	0.34842(2)	0.51257	6.6	0.5	538	−0.51
LA-13	111.5	251.3	181.4	0.1058(3)	0.51280(3)	0.34842(2)	0.51259	6.9	0.6	514	−0.46
LA-14	135.9	207.3	171.6	0.1142(2)	0.51281(5)	0.34841(3)	0.51258	6.6	0.9	535	−0.42
LA-15	116.9	172.4	144.7	0.1008(1)	0.51273(5)	0.34844(3)	0.51253	5.6	0.9	612	−0.49
LA-16	142.4	305.8	224.1	0.1004(2)	0.51278(3)	0.34841(2)	0.51258	6.7	0.6	530	−0.49
mean				0.1032	0.51278	0.34841	0.51257	6.4	0.7	547	−0.48

$(^{143}Nd/^{144}Nd)_i = (^{143}Nd/^{144}Nd)_S - (^{147}Sm/^{144}Nd)_S \times (e^{\lambda(Sm)t} - 1)$; $(^{143}Nd/^{144}Nd)_{CHUR,i} = (^{143}Nd/^{144}Nd)_{CHUR} - (^{147}Sm/^{144}Nd)_{CHUR} \times (e^{\lambda(Sm)t} - 1)$; $\varepsilon Nd(t) = [(^{143}Nd/^{144}Nd)_i/(^{143}Nd/^{144}Nd)_{CHUR,i} - 1] \times 10{,}000$; $f_{Sm/Nd} = [(^{147}Sm/^{144}Nd)s/(^{147}Sm/^{144}Nd)_{CHUR}] - 1$; $T_{DM2} = 1/\lambda(Sm)\ln\{1 + ((^{143}Nd/^{144}Nd)_S - ((^{143}Sm/^{144}Nd)_S - (^{147}Sm/^{144}Nd)_C)(e^{\lambda(Sm)t} - 1))/((^{147}Sm/^{144}Nd)_C - (^{147}Sm/^{144}Nd)_{DM})\}$; where s = sample, $(^{147}Sm/^{144}Nd)CHUR = 0.1967$, $(^{143}Nd/^{144}Nd)CHUR = 0.512638$, $(^{147}Sm/^{144}Nd)DM = 0.2136$, $(^{143}Nd/^{144}Nd)DM = 0.51315$ (Jacobsen and Wasserburg, 1980), $(^{147}Sm/^{144}Nd)C = 0.118$ (Jahn and Condie, 1995), and $\lambda(Sm) = 6.54E-12\ y-1$ (Lugmair and Marti, 1978), t = the emplacement age of the granitoids from Cao et al. (2016a,b).

Relative to other phases, amphibole contains minor contents of MnO (up to 0.48 wt.%). Considering the trace amount of MnO in the whole rock (0.02 to 0.16 wt.%; Cao et al., 2016a), high amount of amphibole in most rocks (8 to 15 vol.% in diorite; 2 to 3 vol.% in granodiorite porphyry; 10 to 15 vol.% in hornblende diorite porphyry; Cao et al., 2016a), and high crystallization temperature of amphibole (mean values of 855 °C in diorite and 972 °C in hornblende diorite porphyry), amphibole crystallization will deplete the Mn content in the residual magma and also in later crystallized apatite. This is consistent with lower fO_2 values in the porphyry (2.4 and 2.8) than that in the diorite (3.3), because amphibole typically crystallizes relatively earlier than apatite in the porphyry relative to diorite, and thus more significantly decrease the apatite Mn contents. Thus, Mn contents in apatite are not suitable for calculating the fO_2 of granitoids in this study.

5.2.3. The variations of $Fe^{3+}/\Sigma Fe$ ratios

The asymmetric shape of the biotite Mössbauer spectra observed in this study was probably caused by sample preparation. Previous Mössbauer analysis on single crystals of biotite reported the same spectra asymmetries that are based on the crystallographic properties of the mineral (Aldridge et al., 1991). Although the samples were all finely ground in the current study, some of the biotite material may have aligned as cleavage flakes and were orientated in the sample holder which might have led to the asymmetric spectroscopic analysis. As a consequence, we assigned the two of the doublets for Fe^{2+} (Db1 and Db2) to fit asymmetrically. The results show relatively consistent $Fe^{3+}/\Sigma Fe$ ratios in both the biotite and amphibole samples (0.039 to 0.098). In addition, the low ratios of $Fe^{3+}/\Sigma Fe$ in biotite (0.039 to 0.093) are in accordance with a previous study on well-preserved unaltered biotite (Gilkes et al., 1972). These results indicate that the $Fe^{3+}/\Sigma Fe$ ratios in the biotite and hornblende samples were well preserved prior to Mössbauer analysis and thus could be used to constrain the oxygen fugacity of magma following previous research (Rancourt et al., 1992; Gunter et al., 2003). Both biotite and amphibole crystallize at a relatively early stage, and whole rock analysis represents the bulk rock composition. Thus, combined with whole rock $Fe^{3+}/\Sigma Fe$ ratios determined by wet chemical methods (Blevin, 2004), systematic variations could be used to discuss the fO_2 evolution of

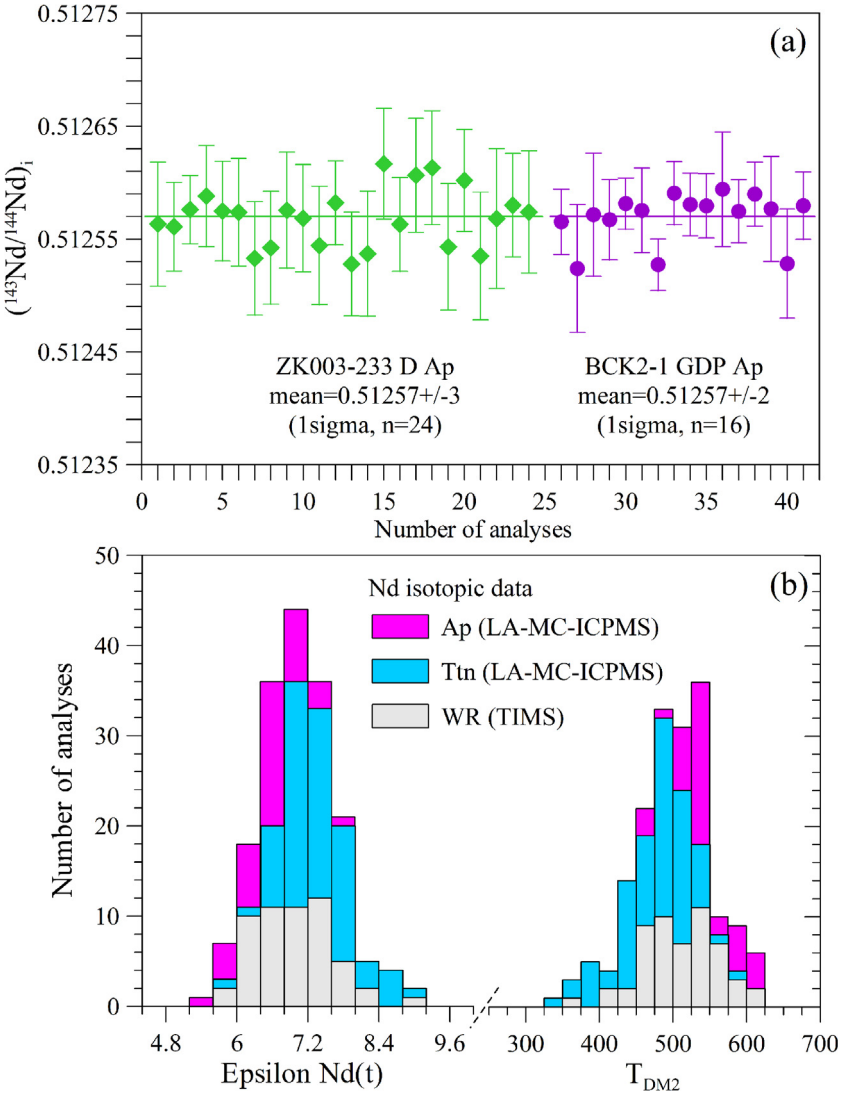

Fig. 7. (a) Diagram showing range of $(^{143}Nd/^{144}Nd)_i$ values of apatite from ZK003-233 diorite (D) and BCK2-1 granodiorite porphyry (GDP). (b) Histograms showing variations of εNd(t) and T_{DM2} for apatite (this study), titanite (from Cao et al., 2015b) and whole rocks (from Shen et al., 2009; Tang et al., 2010; Shen and Pan, 2013; Cao et al., 2016a).

the rock during crystallization. Fig. 11a shows that $Fe^{3+}/\Sigma Fe$ ratios show compatible values but slightly increase from magmatic biotite (0.039 to 0.093, n = 4) and amphibole (0.051 and 0.098) to whole rock (0.06 to 0.28, n = 25), indicating compatible but slightly increasing fO_2 from early to late magmatic stage. According to the results of whole rock $Fe^{3+}/\Sigma Fe$ ratios, fO_2 value of <NNO is estimated on the granitoids (Cao et al., 2016a). Thus, the relatively low ratios of $Fe^{3+}/\Sigma Fe$ in magmatic biotite and amphibole indicate a fO_2 value of <NNO at the early magmatic stage.

Based on the systematic experimental and theoretical calculations of biotite composition (Wones and Eugster, 1965), the proportion of Mg, Fe^{3+}, Fe^{2+} could be used to constrain the oxygen fugacity of rocks. However, the results obtained from the electron microprobe cannot discriminate the ratios of Fe^{3+} and Fe^{2+}, which might introduce a large uncertainty. In this study, we could use the proportion of Fe^{3+} and Fe^{2+} in biotite analyzed by Mössbauer spectroscopy to estimate magma fO_2. Figure 11b shows that the biotite compositions give a fO_2 of <NNO, consistent with the results of $Fe^{3+}/\Sigma Fe$ variations. The fO_2 of <NNO revealed by biotite also show slight lower oxidation state than that revealed by zircon $(Ce/Ce^*)_D$ (fO_2 = ~NNO + 0.6).

5.3. Petrogenesis of granitoids revealed by mineral chemistry

Ore-forming minerals crystallized directly from the magma can record details of the crystallization processes (Davidson and Tepley, 1997; Tepley et al., 2000; Ruprecht and Wörner, 2007; Qin et al., 2009; Boomeri et al., 2010; Shcherbakov et al., 2011; Cao et al., 2012, 2013, 2014c; Bath et al., 2013). The EPMA data indicate that the majority of plagioclase is andesine (An_{26-55}) in the diorite and granodiorite porphyry, but is labradorite (An_{60-69}) in the hornblende diorite porphyry (Fig. 5a). Andesine and labradorite are the feldspar varieties most common in intermediate and mafic igneous rocks, respectively. Similarly, our results also show two distinct types of primary amphibole, type I (Mg-hornblende) in the diorite and granodiorite porphyry, and type II (tschermakite) in the hornblende diorite porphyry (Fig. 4). Mg-hornblende and tschermakite are common constituents of intermediate to felsic and mafic to ultramafic igneous rocks (Mogessie et al., 2000), respectively. Thus, the occurrence of two different types of plagioclase and amphibole in diorite to granodiorite porphyry and in hornblende diorite porphyry suggest two distinct magma sources. In addition, these two types of amphibole show

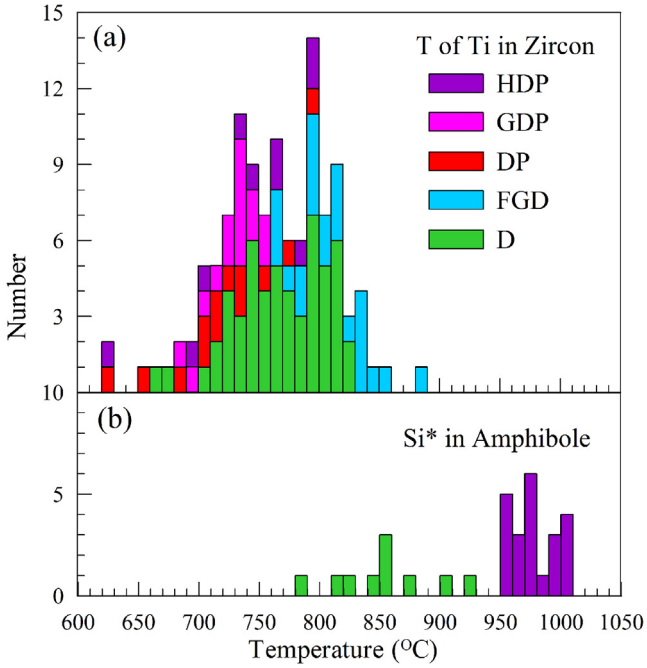

Fig. 8. Histograms of temperature of (a) Ti in zircon calculated according to Watson et al. (2006) and Ferry and Watson (2007), (b) Ti in amphibole calculated according to Otten (1984). The previously published data are from the same source as in Fig. 4.

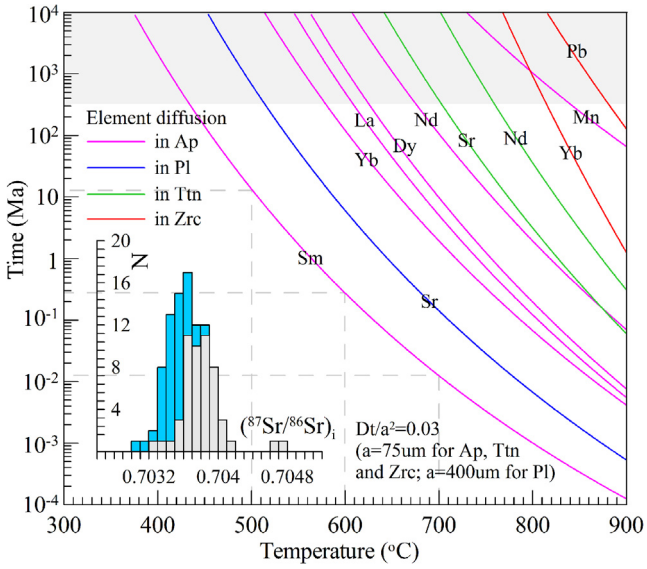

Fig. 9. (a) Summary of conditions for elements diffusional loss in apatite (Ap, a = 75 μm), plagioclase (Pl, a = 400 μm), titanite (Ttn, a = 75 μm) and zircon (Zrc, a = 75 μm). For elemental diffusion data in apatite: Sm from Watson et al. (1985); REE including La-Nd-Dy-Yb from Cherniak (2000); Mn from Cherniak (2005). Sr diffusion data in plagioclase (An42.5) are from Cherniak and Watson (1994). Sr and Nd diffusion data in titanite are from Cherniak (1995). Pb and Yb diffusion data in zircon are from Cherniak and Watson (2001) and Cherniak et al. (1997a). The insert histogram showing the variations of Sr isotopic for whole rock (gray, Shen et al., 2009; Tang et al., 2010; Shen and Pan, 2013; Cao et al., 2016a) and plagioclase (colored, Cao et al., 2014c).

obvious different major element compositions. Fig. 12 shows that the type II amphibole (tschermakite) has lower contents of SiO_2 and MnO but higher contents of Al_2O_3 and Na_2O, relative to the type I amphibole (Mg-hornblende). Furthermore, the trace element compositions of amphiboles show different chondrite-normalized REE patterns with LREE enriched and negative Eu anomalies in type I amphibole but LREE depleted and a lack of Eu anomalies in type II amphibole (Fig. 6c). These observations cannot be accounted for by fractional crystallization and probably indicate the presence of two distinct magmas. Two groups of amphibole with different major element compositions are also recorded in the Black Mountain porphyry system, Philippines (Hollings et al., 2013), and were explained by crystallization of two magmas; one mafic and one felsic. The existence of two distinct magmas is consistent with our previously determined whole rock compositions which show obvious linear correlations between SiO_2 and various elements, and between SiO_2 and Sr-Nd-Pb isotopes (Cao et al., 2016a). The gabbro and granodioritic rocks are interpreted to be end-members (Cao et al., 2016a).

The major and trace element contents from a biotite phenocryst from the granodiorite porphyry (BCK2-1) were analyzed in order to elucidate the detailed crystallization process. Major elements (SiO_2, FeO, MgO, K_2O and TiO_2) are consistent across the phenocryst but trace elements (Zn, Cr, Sc and Sr) show significant variations (Fig. 13). For example, Zn contents initially increase away from the core (71.7 ppm at LA-10) to mantle (140 ppm at LA-9 and 147 ppm at LA-11) and then decrease to the rim (123 ppm at LA-8 and 128 ppm at LA-13) and edge (90.5 ppm at LA-12). Compositional changes in phenocrysts may be caused either by changes in intrinsic variables (such as H_2O content, T, P) or by open system processes (such as magma recharge or contamination) (Davidson and Tepley, 1997). Previous studies of plagioclase showed elemental and isotopic variations consistent with repeated recharge of more mafic magma (with less radiogenic Sr isotopic characteristics) into the felsic magma (with relatively high radiogenic Sr) (Cao et al., 2014c). Considering the analyzed biotite phenocryst and plagioclase grains were obtained on the same thin section, both minerals would be expected to record similar crystallization processes. The restricted Sr-Nd-Hf-O isotopic compositions ($(^{87}Sr/^{86}Sr)_i$ = 0.7036 to 0.7040 and ε_{Nd} (t) = +6.3 to +7.8 for the whole rock, ε_{Hf} (t) = +10.7 to +15.8 and $\delta^{18}O$ = 5.3 to 7.4‰ for zircon; Cao et al., 2016a) exclude significant ancient continental crust or reduced sediment contamination during emplacement as proposed by Shen and Pan (2013). In addition, the increasing $Fe^{3+}/\Sigma Fe$ ratios from magmatic biotite and amphibole to whole rock do not support the contamination or assimilation of organic-bearing sediment during magma emplacement and biogenic origin of CH_4 in hydrothermal fluids as suggested by Shen and Pan (2013), because addition of reduced material will significantly decrease the fO_2 of the magma with crystallization and thus decrease $Fe^{3+}/\Sigma Fe$ ratios in biotite, through amphibole, to whole rock. Thus, our preferred interpretation is that the biotite trace element variations formed by magma recharge or mixing, but not by changes in intrinsic variables, consistent with restricted and similar fO_2 among different phases.

5.4. Source characterisitcs of granitoids revealed by apatite Nd isotope

Due to the immobility of REE in apatite after crystallization (Fig. 9), *in situ* apatite Nd isotopic compositions retain primary values. In addition, due to the high contents of Nd in apatite (e.g., 676 to 1378 ppm in our apatite grains) and the development of modern analytical techniques, *in situ* apatite Nd isotopic composition can be analyzed by LA-MC-ICPMS (e.g., Foster and Vance, 2006; Yang et al., 2008, 2014). Although there is a relatively large uncertainty for the *in situ* Nd isotopic analyses in this study, the 2σ level of 0.4 to 1.2 for εNd(t) is precise enough to constrain the petrogenesis of the related rock. *In situ* Nd isotope signatures have been used, not only to investigate apatite from granitoids (Gregory et al., 2009; Sun et al., 2010), but also from detrital sandstone (Foster and Carter, 2007; Henderson et al., 2010) in order to constrain the source materials. For example, Gregory et al. (2009) and Sun

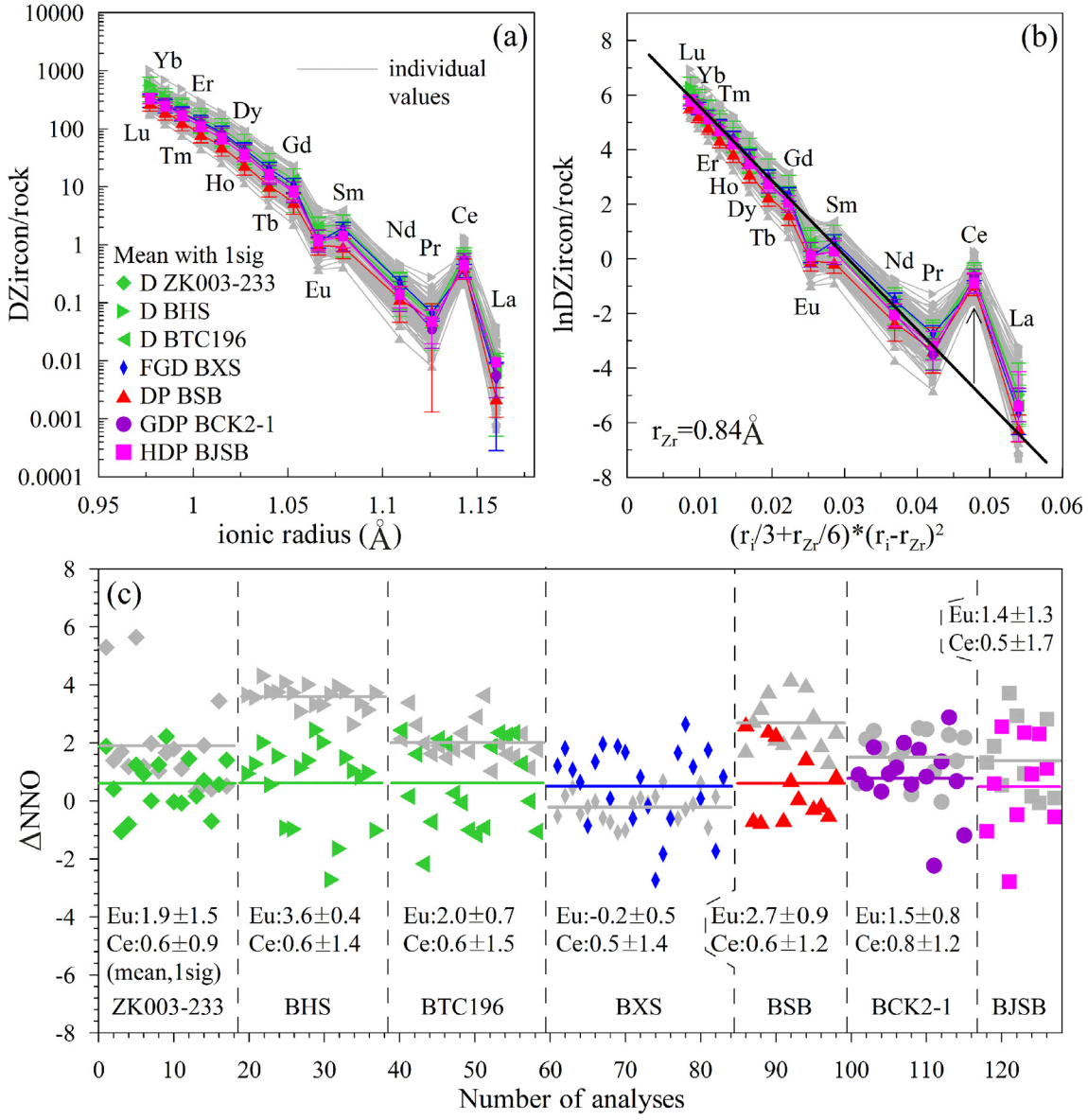

Fig. 10. (a) Calculated zircon/rock distribution coefficients versus ionic radii of the REEs as trivalent cations in eightfold coordination. (b) Natural logarithm of zircon/rock distribution coefficients versus a lattice-strain parameter (modified after Blundy and Wood, 1994; Ballard et al., 2002) for trivalent cations. Linear arrays are predicted according to eightfold coordinates. Results for individual zircon grains are shown in gray and sample mean values are shown in color in (a-b). The positive Ce anomalies relative to the bold black line can be used to estimate the oxygen fugacity. The ionic radii are from Shannon (1976), and rock compositions are from Cao et al., (2016a,b). (c) Distributions of ΔNNO calculated according to the anomalies of Ce (in colored) and Eu (in gray) after Trail et al. (2012) among different samples. The mean values with 1σ are shown in (c).

et al. (2010) combined the *in situ* Nd isotope analysis of apatite and also other REE-rich accessory minerals separated from granitoids with other isotopic analysis to determine the petrogenesis and the source of the host rocks. In this study, all the apatite grains from the ZK003-233 diorite and BCK2-1 granodiorite porphyry show restricted εNd(t) values of 5.9 to 7.6 and 5.6 to 6.9, and also T_{DM2} ages of 460 to 600 Ma and 510 to 620 Ma (Fig. 7b), respectively. These results exhibit similar compositions with those of whole rock (+5.7 to +8.3; Shen et al., 2009; Tang et al., 2010; Shen and Pan, 2013; Cao et al., 2016a) and titanite (+5.8 to +7.8; Cao et al., 2015b) (Fig. 7b). The high and consistent εNd(t) values in different mineral phases (apatite and titanite) and whole rocks indicate an absence of significant sedimentary or ancient continental contamination during magma ascent and/or emplacement. In addition, apatite young T_{DM2} ages of 460 to 620 Ma suggest the source of juvenile, not ancient lower crust, for our ilmenite-series I-type granitoids, consistent with our whole rock geochemical investigation (Cao et al., 2016a).

5.5. Implications for ore-forming processes

The oxidation state of ~ΔNNO + 0.6 estimated by zircon/melt distribution coefficient Ce anomalies is slightly higher than <NNO, determined from early crystallized magmatic biotite compositions which were recalculated based on the results of Mössbauer spectroscopy. Consistent $Fe^{3+}/\Sigma Fe$ ratios in biotite and amphibole reveal similar fO_2 when these minerals crystallized. Combined with the petrologic evidence and crystallization temperature, slightly increasing fO_2 from early to late magmatic stage was observed. This variation might be caused by crystallization of reduced pyrrhotite, which is consistent with the occurrence of pyrrhotite as inclusions in amphibole (Cao et al., 2016a).

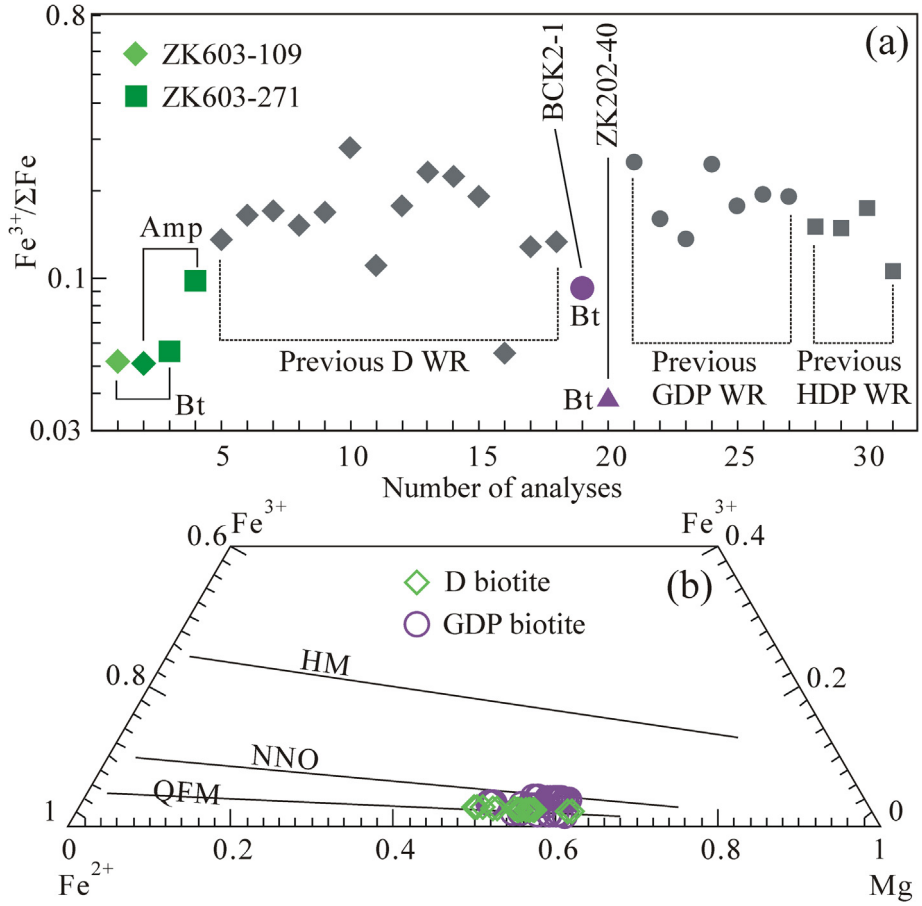

Fig. 11. (a) Variation of $Fe^{3+}/\Sigma Fe$ rations in biotite (Bt) and amphibole (Amp) by Mössbauer spectroscopy, and also whole rock cited from Cao et al. (2016a). (b) Plot of biotite Mg-$Fe3^{+}$-$Fe2^{+}$ diagram after Wones and Eugster (1965), the proportion of Fe^{2+} and Fe^{3+} in biotite calculated according to the results of Mössbauer spectroscopy.

The fO_2 value of <NNO at the time of biotite and amphibole crystallization (mean temperature of 855 °C in diorite and 972 °C in hornblende diorite porphyry) and fO_2 values of ~ΔNNO + 0.6 at the time of zircon crystallization (mean temperature of 717 to 810 °C) is evidence of an obviously lower oxidation state at Baogutu than at typical giant porphyry Cu deposits (>NNO + 2; Mungall, 2002; Richards, 2003; Qin et al., 2014; Shen et al., 2015; Cao et al., 2016b). However, the oxygen fugacity is consistent with that of reduced porphyry Cu deposits (Rowins, 2000; Smith et al., 2012; Cao et al., 2014a) and ilmenite-series I-type granitoids (Cao et al., 2016a). In addition, these values are consistent with our previous results estimated using independent evidence including: (1) mineral assemblage (primary pyrrhotite, predominant magnetite over ilmenite, absence of anhydrite and hematite) (Cao et al., 2014a), (2) the occurrence of titanite replacing ilmenite without magnetite (Cao et al., 2015b), (3) bulk rock magnetic susceptibility with values lower than magnetite-series granitoids (Cao et al., 2016a).

Shen et al. (2010) first discovered the presence of CH_4-rich ore-forming fluids at the Baogutu deposit and ascribed the CH_4 to an upper mantle source. Our detailed fluid inclusion Laser-Raman analyses (Cao et al., 2014a, 2014b, 2015a) supported the widespread occurrence of CH_4 in the ore-forming fluids and indicated that the amount of CO_2 in fluid inclusions in quartz gradually decreased from phenocrystic quartz and interstitial quartz to later hydrothermal vein-type quartz. In addition, the fluid inclusions in apatite included in a biotite phenocryst only contained CO_2 without CH_4 (Cao et al., 2014b), suggesting the presence of CO_2 but not CH_4 during magma crystallization. Based on the results of Takagi and Tsukimura (1997), the carbon species in the magma is controlled by oxidation state of magma. Thus, the fO_2 values at different stage may shed light on the carbon species present during magma crystallization. Takagi and Tsukimura (1997) modeled the fO_2 of magma controlled by the CO_2-CH_4 buffer (CO_2/CH_4 = 1 and 1000; T = 496 to 1155 °C). Fig. 14 shows that the magma fO_2 estimated from biotite compositions and Ce anomalies of zircon/melt distribution coefficients is significantly higher than the buffer of CO_2/CH_4 = 1000, suggesting the CO_2/CH_4 ratio in the magma was >>1000. Thus, the oxidation state (fO_2 variations from <NNO to ~ΔNNO + 0.6) also supports the exclusive occurrence of CO_2 during magma crystallization, and suggests that the CH_4 probably formed from previous magmatic CO_2 during hydrothermal alteration. This is consistent with the results of fluid inclusion CO_2-CH_4 carbon isotopic analyses which indicated that CO_2 was reduced to CH_4 by Fischer-Tropsch type reactions during hydrothermal fluid alteration (Cao et al., 2014b).

Primary amphibole in the deposit was easily altered to actinolite during the Ca-Na silicate alteration stage (Cao et al., 2014a). Fig. 12 shows that the type III actinolite has markedly lower contents of TiO_2, Al_2O_3, FeO, MnO, Na_2O and K_2O than primary type I and II amphibole, suggesting the release of these elements during actinolite alteration. Cao et al. (2014a) observed the widespread occurrence of titanite and albite with minor ilmenite and magnetite accompanying actinolite alteration. Our previous studies have shown that the Baogutu titanite contains minor Al_2O_3 (0.91 to 2.67 wt.%) and FeO (0.18 to 1.47 wt.%), in addition to major SiO_2, TiO_2 and CaO (Cao et al., 2015b), and that ilmenite contains a moderate amount of MnO (2.66 to 5.30 wt.%) (Cao et al.,

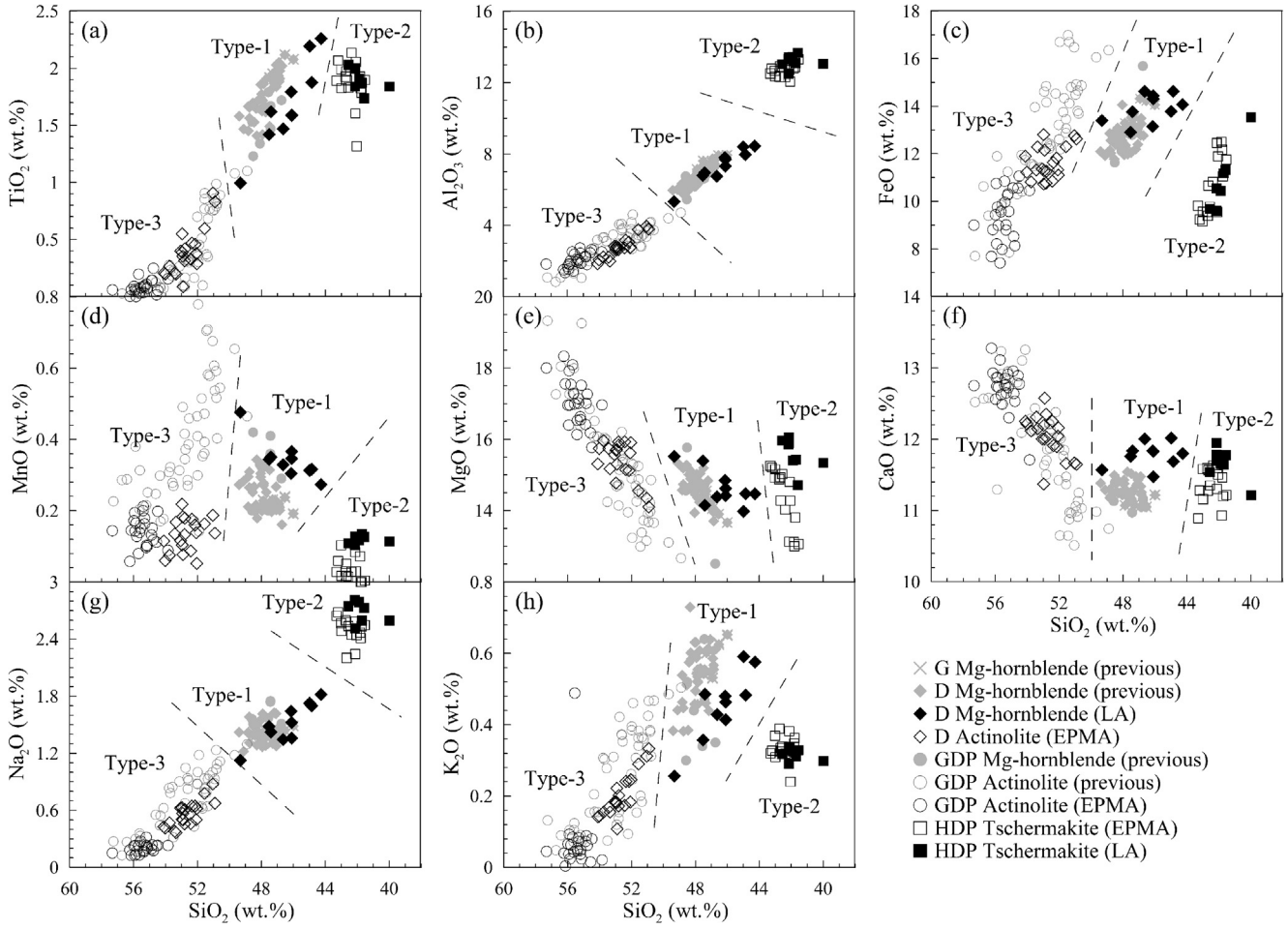

Fig. 12. Plots of SiO_2 versus TiO_2 (a), Al_2O_3 (b), FeO (c), MnO (d), MgO (e), CaO (f), Na_2O (g) and K_2O (h) for calcic-amphiboles from Baogutu deposit, showing three different types (Type-1, Type-2 and Type-3) of calcic-amphibole. The previously published data are the same as in Fig. 4.

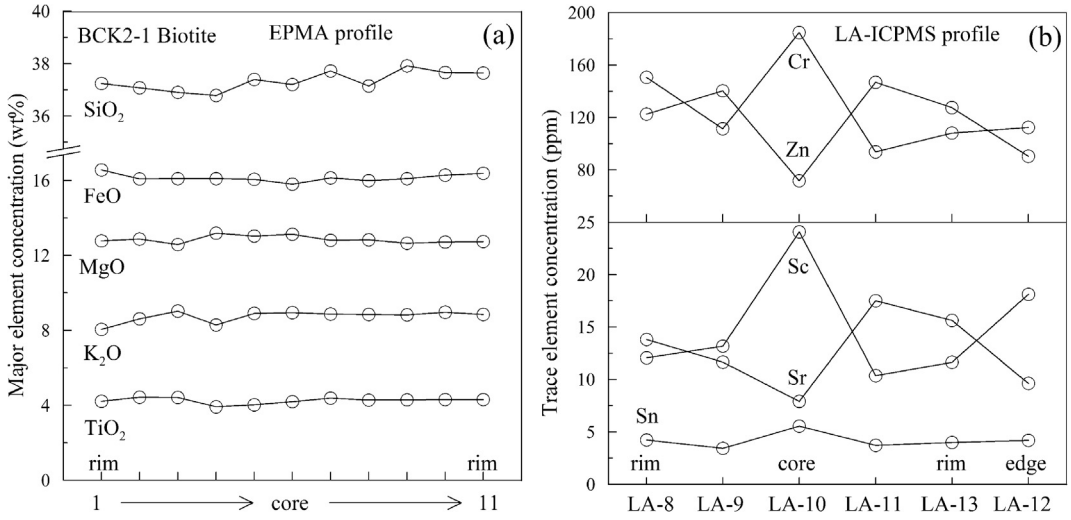

Fig. 13. EPMA profile (a) and LA-ICPMS profile for biotite phenocryst in Fig. 2g, showing the variations of major elements (SiO_2, FeO, MgO, K_2O and TiO_2) and trace elements (Cr, Zn, Sc, Sr and Sn).

2015b). The high temperature hydrothermal fluids may have provided the Si and Ca (Von Damm, 2000), and dissolved K which likely precipitated as K-feldspar during subsequent potassic alteration. Thus, the mineral assemblage of actinolite, titanite, albite with minor ilmenite and magnetite is interpreted to reflect compositional dissolution and re-precipitation.

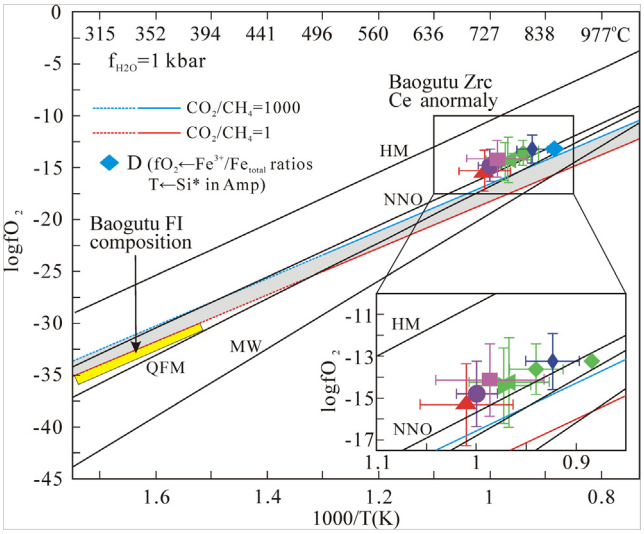

Fig. 14. logfO_2 versus 1000/T showing the oxygen fugacity of zircon based on Ce anomalies after Trail et al. (2012) and biotite based on Mg-Fe^{3+}-Fe^{2+} compositions (after Wones and Eugster, 1965) and Si* in Amp thermometry (Ridolfi et al., 2010), the CO_2-CH_4 buffer lines (in color) from Takagi and Tsukimura (1997), the mineral-mineral buffer curves (in dark) including Fe_2O_3-Fe_3O_4 (HM), Ni-NiO (NNO), SiO_2-Fe_2SiO_4-Fe_3O_4 (QFM) from Eugster and Wones (1962), and Fe_3O_4-FeO (MW) from Darken and Gurry (1945). The CO_2-CH_4 buffer curves with dotted lines at lower temperatures are extrapolated from Takagi and Tsukimura (1997). Our previous Laser-Raman microprobe analytical results (Cao et al., 2014a, 2014b, 2015a) show predominant CH_4 over CO_2 in ore-forming fluids with CO_2/CH_4 ratios far less than 1, suggesting the oxygen fugacity <CO_2/CH_4 = 1 buffer. The legends of zircon are the same as Fig. 10.

6. Conclusions

(1) The results of Mössbauer spectroscopy show consistently low $Fe^{3+}/\Sigma Fe$ ratios in both biotite and amphibole samples (3.9 to 9.8%), which is slightly lower than whole rock ratios, indicating a slight increase in oxygen fugacity during magma crystallization. Recalculated biotite compositions according to the $Fe^{3+}/\Sigma Fe$ ratios show fO_2 values of <NNO, a slightly lower oxidation state than that indicated from zircon Ce anomalies (~ΔNNO + 0.6).

(2) The Baogutu granitoids contain different types of plagioclase (andesine An_{26-55} versus labradorite An_{60-69}) and amphibole (Mg-hornblende versus tschermakite) with distinct elemental compositions, indicating two distinct magma sources. Significant trace elemental variations in biotite profiles may reflect the mixing of two distinct magmas.

(3) *In situ* apatite grains show restricted εNd(t) values of 5.6 to 7.6 and T_{DM2} ages of 460 to 620 Ma, indicating the absence of significant sedimentary or ancient continental contamination and a juvenile lower crust source.

(4) The fO_2 variations from <NNO to ~ΔNNO + 0.6 consistently require the exclusive occurrence of CO_2 without CH_4 at the magmatic stage, which implies transformation of CH_4 from magmatic CO_2 at hydrothermal alteration. The alteration of primary amphibole likely released Ti, Al, Fe, Mn, Na and K into the hydrothermal fluids.

Acknowledgements

The authors are greatly indebted to James M. Byrne for his assistance with Mössbauer spectroscopy analyses, Qian Mao and YuGuang Ma for their assistance with EPM analyses, YueHeng Yang and Yang Li for assistance with LA-(MC)-ICPMS trace element and Nd isotopic analyses. In particular, we express our gratitude to XiaoLei Wang and another anonymous reviewer and the Editor Prof. Franco Pirajno and TaoFa Zhou for their constructive comments and excellent suggestions that helped to improve the manuscript. This research was financially supported by National Natural Sciences Foundation of China (41402081, 41390444 and 41672090), International Postdoctoral Exchange Fellowship Program of China (20150085) and Special Fund for Scientific Research in the Public Interest of Ministry of Land and Resources of China (201411024-5).

Appendix A. Supplementary data

Supplementary data associated with this article can be found, in the online version, at http://dx.doi.org/10.1016/j.oregeorev.2017.02.033.

References

Aldridge, L.P., Finch, J., Gainsford, G.J., Patterson, K.H., Tennant, W.C., 1991. Single crystal Mössbauer studies of 1M biotite. Phys. Chem. Miner. 17, 583–590.
Audétat, A., Pettke, T., Dolejš, D., 2004. Magmatic anhydrite and calcite in the ore-forming quartz-monzodiorite magma at Santa Rita, New Mexico (USA): genetic constraints on porphyry-Cu mineralization. Lithos 72, 147–161.
Ballard, J.R., Palin, M.J., Campbell, I.H., 2002. Relative oxidation states of magmas inferred from Ce (IV)/Ce (III) in zircon: application to porphyry copper deposits of northern Chile. Contrib. Miner. Petrol. 144, 347–364.
Bath, A.B., Walshe, J.L., Cloutier, J., Verrall, M., Cleverley, J.S., Pownceby, M.I., Macrae, C.M., Wilson, N.C., Tunjic, J., Nortje, G.S., 2013. Biotite and apatite as tools for tracking pathways of oxidized fluids in the Archean east repulse gold deposit, Australia. Econ. Geol. 108, 667–690.
Blevin, P.L., 2004. Redox and compositional parameters for interpreting granitoid metallogeny of eastern Australia: implications for gold-rich ore systems. Resour. Geol. 54, 241–252.
Blundy, J., Wood, B., 1994. Prediction of crystal melt partition coefficients from elastic moduli. Nature 372, 452–454.
Boomeri, M., Nakashima, K., Lentz, D.R., 2010. The Sarcheshmeh porphyry copper deposit, Kerman, Iran: a mineralogical analysis of the igneous rocks and alteration zones including halogen element systematics related to Cu mineralization processes. Ore Geol. Rev. 38, 367–381.
Cao, M.J., Li, G.M., Qin, K.Z., Seitmuratova, E.Y., Liu, Y.S., 2012. Major and trace element characteristics of apatites in granitoids from central Kazakhstan: implications for petrogenesis and mineralization. Resour. Geol. 62, 63–83.
Cao, M.J., Zhou, Q.F., Qin, K.Z., Tang, D.M., Evans, N.J., 2013. The tetrad effect and geochemistry of apatite from the Altay Koktokay No. 3 pegmatite, Xinjiang, China: implications for pegmatite petrogenesis. Mineral. Petrol. 107, 985–1005.
Cao, M.J., Qin, K.Z., Li, G.M., Jin, L.Y., Evans, N.J., Yang, X.R., 2014a. Baogutu: an example of reduced porphyry Cu deposit in western Junggar. Ore Geol. Rev. 56, 159–180.
Cao, M.J., Qin, K.Z., Li, G.M., Evans, N.J., Jin, L.Y., 2014b. Abiogenic Fischer-Tropsch synthesis of methane at the Baogutu reduced porphyry copper deposit, western Junggar, NW-China. Geochim. Cosmochim. Acta 141, 179–198.
Cao, M.J., Qin, K.Z., Li, G.M., Yang, Y.H., Evans, N.J., Zhang, R., Jin, L.Y., 2014c. Magmatic process recorded in plagioclase at the Baogutu reduced porphyry Cu deposit, western Junggar, NW-China. J. Asian Earth Sci. 82, 136–150.
Cao, M.J., Qin, K.Z., Li, G.M., Evans, N.J., He, H.Y., Jin, L.Y., 2015a. A mixture of mantle and crustal derived He-Ar-C-S ore-forming fluids at the Baogutu reduced porphyry Cu deposit, Western Junggar. J. Asian Earth Sci. 98, 188–197.
Cao, M.J., Qin, K.Z., Li, G.M., Evans, N.J., Jin, L.Y., 2015b. *In situ* LA-(MC)-ICP-MS trace element and Nd isotopic compositions and genesis of polygenetic titanite from the Baogutu reduced porphyry Cu deposit, Western Junggar, NW China. Ore Geol. Rev. 65, 940–954.
Cao, M.J., Qin, K.Z., Li, G.M., Evans, N.J., Hollings, P., Jin, L.Y., 2016a. Genesis of ilmenite-series I-type granitoids at the Baogutu reduced porphyry Cu deposit, western Junggar, NW-China. Lithos 246–247, 13–30.
Cao, M.J., Li, G.M., Qin, K.Z., Evans, N.J., Seitmuratova, E.Y., 2016b. Assessing the magmatic affinity and petrogenesis of granitoids at the giant Aktogai porphyry Cu deposit, central Kazakhstan. Am. J. Sci. 316, 614–668.
Chandra, R., Tripathi, R., Lokanathan, S., 1978. Search for anisotropy of Mössbauer absorption in biotite. Phys. Status Solidi B 88, 633–637.
Cherniak, D.J., Watson, E.B., 1994. A study of strontium diffusion in plagioclase using Rutherford backscattering spectroscopy. Geochim. Cosmochim. Acta 58, 5179–5190.
Cherniak, D., 1995. Sr and Nd diffusion in titanite. Chem. Geol. 125, 219–232.
Cherniak, D.J., Hanchar, J.M., Watson, E.B., 1997a. Rare-earth diffusion in zircon. Chem. Geol. 134, 289–301.
Cherniak, D.J., Hanchar, J.M., Watson, E.B., 1997b. Diffusion of tetravalent cations in zircon. Contrib. Miner. Petrol. 127, 383–390.
Cherniak, D., 2000. Rare earth element diffusion in apatite. Geochim. Cosmochim. Acta 64, 3871–3885.

Cherniak, D.J., Watson, E.B., 2001. Pb diffusion in zircon. Chem. Geol. 172, 5–24.
Cherniak, D., 2005. Uranium and manganese diffusion in apatite. Chem. Geol. 219, 297–308.
Crank, J., 1975. The Mathematics of Diffusion. Oxford University Press, UK.
Dai, H.W., Shen, P., Shen, Y.C., Pan, H.D., Liu, T.B., Meng, L., Guan, W.N., 2010. Mineralogy of ore-bearing porphyries in the Baogutu copper-gold belt of West Junggar and its geological significance. Xinjiang Geol. 28, 440–447 (in Chinese with English abstract).
Darken, L.S., Gurry, R.W., 1945. The system iron-oxygen. I. The Wüstite Field and Related Equilibria. J. Am. Chem. Soc. 67, 1398–1412.
Davidson, J.P., Tepley, F.J., 1997. Recharge in volcanic systems: evidence from isotope profiles of phenocrysts. Science 275, 826–829.
Drake, M.J., Weill, D.F., 1975. Partition of Sr, Ba, Ca, Y, Eu^{2+}, Eu^{3+}, and other REE between plagioclase feldspar and magmatic liquid: an experimental study. Geochim. Cosmochim. Acta 39, 689–712.
Eugster, H.P., Wones, D.R., 1962. Stability relations of the ferruginous biotite, annite. J. Petrol. 3, 82–125.
Ferry, J.M., Watson, E.B., 2007. New thermodynamic models and revised calibrations for the Ti-in-zircon and Zr-in-rutile thermometers. Contrib. Miner. Petrol. 154, 429–437.
Foster, G.L., Carter, A., 2007. Insights into the patterns and locations of erosion in the Himalaya–a combined fission-track and *in situ* Sm-Nd isotopic study of detrital apatite. Earth Planet. Sci. Lett. 257, 407–418.
Foster, G.L., Vance, D., 2006. In situ Nd isotopic analysis of geological materials by laser ablation MC-ICP-MS. J. Anal. At. Spectrom. 21, 288–296.
Gilkes, R., Young, R., Quirk, J., 1972. Oxidation of ferrous iron in biotite. Nature 236, 89–91.
Gregory, C.J., McFarlane, C.R.M., Hermann, J., Rubatto, D., 2009. Tracing the evolution of calc-alkaline magmas: In-situ Sm-Nd isotope studies of accessory minerals in the Bergell Igneous Complex, Italy. Chem. Geol. 260, 73–86.
Griffin, W.L., Powell, W.J., Pearson, N.J., O'Reilly, S.Y., 2008. GLITTER: data reduction software for laser ablation ICP-MS. In: Sylvester, P. (Ed.), Laser Ablation-ICP-MS in the Earth Sciences. Mineralogical Association of Canada, pp. 204–207. Short Course 40.
Gunter, M.E., Dyar, M.D., Twamley, B., Foit, F.F., Cornelius, S., 2003. Composition, $Fe^{3+}/\Sigma Fe$, and crystal structure of non-asbestiform and asbestiform amphiboles from Libby, Montana, USA. Am. Mineral. 88, 1970–1978.
Hanchar, J.M., Finch, R.J., Hoskin, P.W., Watson, E.B., Cherniak, D.J., Mariano, A.N., 2001. Rare earth elements in synthetic zircon: Part 1. Synthesis, and rare earth element and phosphorus doping. Am. Mineral. 86, 667–680.
Hedenquist, J., Lowenstern, J., 1994. The role of magmas in the formation of hydrothermal ore deposits. Nature 370, 519–527.
Henderson, A.L., Foster, G.L., Najman, Y., 2010. Testing the application of in situ Sm-Nd isotopic analysis on detrital apatites: a provenance tool for constraining the timing of India-Eurasia collision. Earth Planet. Sci. Lett. 297, 42–49.
Hollings, P., Sweet, G., Baker, M., Cooke, D., Fiedman, R., 2013. Tectonomagmatic controls on porphyry mineralization: Geochemical evidence from the Black Mountain porphyry system, Philippines. In: Colporn, M., Bissig, T., Rusk, B.G., Thompson, J.F.H. (Eds.), Tectonics, Metallogeny, and Discovery: The North American Cordillera and Similar Accretionary Settings. Society of Economic Geologists, pp. 301–335. Special Publication 17.
Jacobsen, S., Wasserburg, G., 1980. Sm-Nd isotopic evolution of chondrites. Earth Planet. Sci. Lett. 50, 139–155.
Jahn, B.M., 2004. The Central Asian Orogenic Belt and growth of the continental crust in the Phanerozoic. Geological Society, London. Special Publications 226, 73–100.
Jahn, B.M., Condie, K.C., 1995. Evolution of the Kaapvaal Craton as viewed from geochemical and Sm-Nd isotopic analyses of intracratonic pelites. Geochim. Cosmochim. Acta 59, 2239–2258.
Larese-Casanova, P., Haderlein, S.B., Kappler, A., 2010. Biomineralization of lepidocrocite and goethite by nitrate-reducing Fe(II)-oxidizing bacteria: Effect of pH, bicarbonate, phosphate and humic acids. Geochim. Cosmochim. Acta 74, 3721–3734.
Leake, B.E., Woolet, A.R., Arps, C.E.S., Birch, W.D., Gilbert, M.C., Grice, J.D., Hawthorne, F.C., Kato, A., Kisch, H.J., Krivovichev, E.A., 1997. Nomenclature of amphiboles: report of the subcommittee on amphiboles of the International Mineralogical Association, Commission on New Minerals and Mineral Names. Can. Mineral. 35, 219–246.
Li, G.M., Cao, M.J., Qin, K.Z., Evans, N.J., McInnes, B.I.A., Liu, Y.S., 2014. Thermal-tectonic history of the Baogutu porphyry Cu deposit, West Junggar as constrained from zircon U-Pb, biotite Ar/Ar and zircon/apatite (U–Th)/He dating. J. Asian Earth Sci. 79, 741–758.
Lugmair, G.W., Marti, K., 1978. Lunar initial $^{143}Nd/^{144}Nd$: differential evolution of the lunar crust and mantle. Earth Planet. Sci. Lett. 39, 349–357.
Luo, Y., Ayers, J.C., 2009. Experimental measurements of zircon/melt trace-element partition coefficients. Geochim. Cosmochim. Acta 73, 3656–3679.
Miles, A.J., Graham, C.M., Hawkesworth, C.J., Gillespie, M.R., Hinton, R.W., Bromiley, G.D., 2014. Apatite: A new redox proxy for silicic magmas? Geochim Cosmochim Acta 132, 101–119.
Mitra, S., Bansal, C., 1975. ^{57}Fe Mössbauer study of volcanic hornblende. Chem. Phys. Lett. 30, 403–405.
Mogessie, A., Hauzenberger, C.A., Hoinkes, G., Felfernig, A., Stumpfl, E., Bjerg, E., Kostadinoff, J., 2000. Genesis of platinum-group minerals in the Las Aguilas mafic-ultramafic rocks, San Luis Province, Argentina: textural, chemical and mineralogical evidence. Mineral. Petrol. 68, 85–114.
Muehe, E.M., Obst, M., Hitchcock, A., Tyliszczak, T., Behrens, S., Schroeder, C., Byrne, J.M., Michel, F.M., Kraemer, U., Kappler, A., 2013. Fate of Cd during microbial Fe (III) mineral reduction by a novel and Cd-tolerant Geobacter species. Environ. Sci. Technol. 47, 14099–14109.
Mungall, J., 2002. Roasting the mantle: slab melting and the genesis of major Au and Au-rich Cu deposits. Geology 30, 915–918.
Nachit, H., Ibhi, A., Abia, E., Ben Ohoud, M., 2005. Discrimination between primary magmatic biotites, reequilibrated biotites and neoformed biotites. Comptes Rendus Geosci. 337, 1415–1420.
Onuma, N., Higuchi, H., Wakita, H., Nagasawa, H., 1968. Trace element partition between two pyroxenes and the host lava. Earth Planet. Sci. Lett. 5, 47–51.
Otten, M.T., 1984. The origin of brown hornblende in the Artfjället gabbro and dolerites. Contrib. Miner. Petrol. 86, 189–199.
Parat, F., Holtz, F., 2005. Sulfur partition coefficient between apatite and rhyolite: the role of bulk S content. Contrib. Miner. Petrol 150, 643–651.
Qin, K.Z., Ishihara, S., 1998. On the possibility of porphyry copper mineralization in Japan. Int. Geol. Rev. 40, 539–551.
Qin, K.Z., Zhang, L.C., Ding, K.S., Xu, Y.X., Tang, D.M., Xu, X.W., Ma, T.L., Li, G.M., 2009. Mineralization type, petrogenesis of ore-bearing intrusions and mineralogical characteristics of Sanchakou copper deposits in eastern Tianshan. Acta Petrol. Sin. 25, 845–861 (in Chinese with English abstract).
Qin, K.Z., Xia, D., Li, G.M., Xiao, B., Duo, J., Jiang, G.W., Zhao, J.X., 2014. Qulong porphyry-skarn type Cu-Mo Deposit, Tibet. Science Press, Beijing. 1–316 (in Chinese).
Rancourt, D., Ping, J., 1991. Voigt-based methods for arbitrary-shape static hyperfine parameter distributions in Mössbauer spectroscopy. Nucl. Instrum. Methods Phys. Res., Sect. B 58, 85–97.
Rancourt, D.G., Dang, M.Z., Lalonde, A.E., 1992. Mössbauer spectroscopy of tetrahedral Fe^{3+} in trioctahedral micas. Am. Mineral. 77, 34–43.
Richards, J., 2003. Tectono-magmatic precursors for porphyry Cu-(Mo-Au) deposit formation. Econ. Geol. 98, 1515–1533.
Ridolfi, F., Renzulli, A., Puerini, M., 2010. Stability and chemical equilibrium of amphibole in calc-alkaline magmas: an overview, new thermobarometric formulations and application to subduction-related volcanoes. Contrib. Miner. Petrol. 160, 45–66.
Rowins, S.M., 2000. Reduced porphyry copper-gold deposits: a new variation on an old theme. Geology 28, 491–494.
Ruprecht, P., Wörner, G., 2007. Variable regimes in magma systems documented in plagioclase zoning patterns: El Misti stratovolcano and Andahua monogenetic cones. J. Volcanol. Geoth. Res. 165, 142–162.
Shannon, R., 1976. Revised effective ionic radii and systematic studies of interatomic distances in halides and chalcogenides. Acta Crystallogr. A 32, 751–767.
Shcherbakov, V., Plechov, P., Izbekov, P., Shipman, J., 2011. Plagioclase zoning as an indicator of magma processes at Bezymianny Volcano, Kamchatka. Contrib. Miner. Petrol. 162, 83–99.
Shen, P., Hattori, K., Pan, H., Jackson, S., Seitmuratova, E., 2015. Oxidation condition and metal fertility of granitic magmas: zircon trace-element data from porphyry Cu deposits in the Central Asian Orogenic Belt. Econ. Geol. 110, 1861–1878.
Shen, P., Pan, H., 2013. Country-rock contamination of magmas associated with the Baogutu porphyry Cu deposit, Xinjiang, China. Lithos 177, 451–469.
Shen, P., Shen, Y.C., Liu, T.B., Meng, L., Dai, H.W., Yang, Y.H., 2009. Geochemical signature of porphyries in the Baogutu porphyry copper belt, western Junggar, NW China. Gondwana Res. 16, 227–242.
Shen, P., Shen, Y., Wang, J., Zhu, H., Wang, L., Meng, L., 2010. Methane-rich fluid evolution of the Baogutu porphyry Cu-Mo-Au deposit, Xinjiang, NW China. Chem. Geol. 275, 78–98.
Shen, P., Shen, Y., Pan, H., Li, X.-H., Dong, L., Wang, J., Zhu, H., Dai, H., Guan, W., 2012. Geochronology and isotope geochemistry of the Baogutu porphyry copper deposit in the West Junggar region, Xinjiang, China. J. Asian Earth Sci. 49, 99–115.
Sillitoe, R.H., 2010. Porphyry copper systems. Econ. Geol. 105, 3–41.
Smith, C.M., Canil, D., Rowins, S.M., Friedman, R., 2012. Reduced granitic magmas in an arc setting: the Catface porphyry Cu–Mo deposit of the Paleogene Cascade Arc. Lithos 154, 361–373.
Song, H.X., Liu, Y.L., Qu, W.J., Song, B., Zhang, R., Cheng, Y., 2007. Geological characters of Baogutu porphyry copper deposit in Xinjiang, NW China. Acta Petrol. Sin. 23, 1981–1988 (in Chinese with English abstract).
Sun, J.F., Yang, J.H., Wu, F.Y., Li, X.H., Yang, Y.H., Xie, L.W., Wilde, S.A., 2010. Magma mixing controlling the origin of the Early Cretaceous Fangshan granitic pluton, North China Craton: *In situ* U-Pb age and Sr-, Nd-, Hf- and O-isotope evidence. Lithos 120, 421–438.
Takagi, T., Tsukimura, K., 1997. Genesis of oxidized- and reduced-type granites. Econ. Geol. 92, 81–86.
Tang, G.J., Wang, Q., Wyman, D.A., Li, Z.X., Zhao, Z.H., Jia, X.H., Jiang, Z.Q., 2010. Ridge subduction and crustal growth in the Central Asian Orogenic Belt: evidence from Late Carboniferous adakites and high-Mg diorites in the western Junggar region, northern Xinjiang (west China). Chem. Geol. 277, 281–300.
Taylor, S.R., McLennan, S.M., 1985. The Continental Crust: Its Composition and Evolution. Blackwell Scientific Publications, Oxford, p. 312.
Tepley, F.J., Davidson, J.P., Tilling, R.I., Arth, J.G., 2000. Magma mixing, recharge and eruption histories recorded in plagioclase phenocrysts from El Chichón volcano, Mexico. J. Petrol. 41, 1397–1411.
Trail, D., Bruce Watson, E., Tailby, N.D., 2012. Ce and Eu anomalies in zircon as proxies for the oxidation state of magmas. Geochim. Cosmochim. Acta 97, 70–87.
Von Damm, K., 2000. Chemistry of hydrothermal vent fluids from 9–10 N, East Pacific Rise:"Time zero", the immediate posteruptive period. J. Geophys. Res. 105, 11203–11222.

Watson, E.B., Harrison, T.M., Ryerson, F.J., 1985. Diffusion of Sm, Sr, and Pb in fluorapatite. Geochim. Cosmochim. Acta 49, 1813–1823.
Watson, E.B., Wark, D.A., Thomas, J.B., 2006. Crystallization thermometers for zircon and rutile. Contrib. Miner. Petrol. 151, 413–433.
Wei, F., Liu, Y.L., Guo, G.L., Zhang, R., Zhang, Y.X., Wang, J., 2009. Characteristics and genesis significance of Titanium minerals of Baogutu porphyry copper deposit, Xinjiang. Acta Petrol. Sin. 25, 645–649 (in Chinese with English abstract).
Wei, S.N., Zhu, Y.F., 2010. Emplacement of the intermediate and acid magmatic rocks in Xinjiang: constraints from the *P-T-fO*$_2$ and geochemistry. Acta Geol. Sinica 84, 1017–1029 (in Chinese with English abstract).
Xie, L.W., Zhang, Y.B., Zhang, H.H., Sun, J.F., Wu, F.Y., 2008. *In situ* simultaneous determination of trace elements, U-Pb and Lu-Hf isotopes in zircon and baddeleyite. Chin. Sci. Bull. 53, 1565–1573.
Wones, D.R., Eugster, H.P., 1965. Stability of biotite: experiment, theory, and application. Am. Mineral. 50, 1228–1272.
Yang, Y.H., Sun, J.F., Xie, L.W., Fan, H.R., Wu, F.Y., 2008. *In situ* Nd isotopic measurement of natural geological materials by LA-MC-ICPMS. Chin. Sci. Bull. 53, 1062–1070.
Yang, Y.H., Wu, F.Y., Yang, J.H., Chew, D.M., Xie, L.W., Chu, Z.Y., Zhang, Y.B., Huang, C., 2014. Sr and Nd isotopic compositions of apatite reference materials used in U-Th–Pb geochronology. Chem. Geol. 385, 35–55.
Zhang, L.F., Xian, W.S., Sun, M., 2004. Petrogenesis of charnockites from Western Junggar, Xinjiang, China. XInjiang Geol. 22, 36–42 (in Chinese with English abstract).
Zhang, R., Zhang, Y.X., Dong, G.S., Wang, J., Li, L.Q., 2006. Major breakthrough in copper exploration in the Baogutu porphyry copper deposit, western Junggar, Xinjiang, and its significance. Geol. China 33, 1354–1360 (in Chinese with English abstract).